Non-Hermitian swallowtail catastrophe revealing transitions among diverse topological singularities

Jing Hu[1,#], Ruo-Yang Zhang[1,#], Yixiao Wang[1], Xiaoping Ouyang[2], Yifei Zhu[3]*, Hongwei Jia[1,4]*, C. T. Chan[1,]*

[1]Department of Physics, the Hong Kong University of Science and Technology, Clear Water Bay, Kowloon, Hong Kong, China

[2]School of Materials Science and Engineering, Xiangtan University, Xiangtan, Hunan, China

[3]Department of Mathematics, Southern University of Science and Technology, Shenzhen, Guangdong, China

[4]Institute for Advanced Study, the Hong Kong University of Science and Technology, Clear Water Bay, Kowloon, Hong Kong, China

[#]These authors contributed equally to this work

Exceptional points are a unique feature of non-Hermitian systems, at which the eigenvalues and corresponding eigenstates of a Hamiltonian coalesce. Many intriguing physical phenomena arise from the topology of exceptional points, such as bulk-Fermi arcs and the braiding of eigenvalues. Here, we report that a structurally richer degeneracy morphology, known as the swallowtail catastrophe in singularity theory, can naturally exist in non-Hermitian systems with both parity–time and pseudo-Hermitian symmetries. For the swallowtail, three different types of singularity exist at the same time and interact with each other — an isolated nodal line, a pair of

exceptional lines of order three and a nondefective intersection line. Although these singularities seem independent, they are stably connected at a single point — the vertex of the swallowtail — through which transitions can occur. We implement such a system in a nonreciprocal circuit and experimentally observe the degeneracy features of the swallowtail. Based on the frame rotation and deformation of eigenstates, we further demonstrate that the various transitions are topologically protected.

Main: In recent years, non-Hermitian systems have attracted a great deal of interest. A main goal is to address the ubiquitous open quantum systems that undergo energy exchange with the surrounding environment via the imaginary part of their eigenenergies.[1–12] Degenerate singularities in band structures are similar to topological defects in real space. Well-known singularities in Hermitian systems are Weyl/Dirac points and nodal lines[13–18], and their associated phenomena, such as topological edge modes[13,18] and chiral Landau levels[16], have been fully explored. In non-Hermitian systems, the complex nature of eigenvalues results in more exotic singularities such as exceptional points, at which two or more eigenstates coalesce. Exceptional points can carry fractional topological invariants, which not only enrich the topological classes in band theory, but also induce more intriguing physical consequences, such as “bulk Fermi arcs”[2,3] and braiding of eigenvalues[10]. In addition, the skin effect, which is associated with the point gaps in non-Hermitian bands, is also a unique feature of non-Hermitian systems.[19–21]

In non-Hermitian systems with parity–time (PT) symmetry or chiral symmetry, exceptional surfaces (ESs) can stably exist as singular hypersurfaces in three-dimensional (3D) parameter space, acting as boundaries between exact and broken phases.[22–24] Remarkably, as subspaces of the parameter space, these ESs can exhibit numerous new singularities, such as high-order exceptional points (or lines) appearing as cusps[6,9] and nondefective degeneracies that are intersections of ESs[8,11,12]. The coexistence of diverse singularities brings the possibility that these singularities can be associated with each other. However, previous works have commonly focused on a single type. The transitions among different types, as well as the underlying topological structure, remain largely unexplored.

In Hermitian systems with PT symmetry[17,25–27] (the corresponding Hamiltonians are real Hermitian matrices), the eigenstates were previously reported to be real and orthogonal and to form the orthonormal basis of a Euclidean-like space.[17] The nodal lines in the band structure manifest as topological obstructions of the eigenstate frames, around which the eigenstates rotate in a way characterized by non-Abelian quaternion topological charges,[17] which has been experimentally observed in a recent work.[18] Here, by expanding our scope to non-Hermitian systems, in particular those with PT symmetry and an additional η-pseudo-Hermitian symmetry, the eigenstates form a Minkowski-like orthogonal basis in which the vectors inhabit a space comparable to the Riemann space used in general relativity. As a result, a more exotic and structurally much richer degeneracy morphology emerges, known as the *swallowtail catastrophe* in singularity theory[28]. The swallowtail is one of the elementary catastrophes in Arnold's ADE classification[28–30] and has been widely applied in many branches of physics and engineering, ranging from mechanics[31] to caustics of light[32]. However, it has never been studied in eigenvalue dispersions. Here, we discover for the first time that the swallowtail catastrophe, which naturally exists in the parameter space of non-Hermitian systems with PT symmetry together with a pseudo-Hermitian symmetry, encompasses degeneracy lines of three different types. In addition to a nodal line (NL) isolated from ESs (similar to the NLs in Hermitian systems), the swallowtail also has a pair of exceptional lines of order three (EL3) and a nondefective intersection line (NIL), which lie entirely on the ESs. Both the NL and NIL are lines of diabolic points with two linearly independent degenerate eigenstates. The difference is that the NL is isolated from ESs, whereas the NIL is not isolated, as it is the intersection line of ESs. Surprisingly, these seemingly independent types of degeneracy lines are stably connected at a meeting point (MP) on the swallowtail, revealing interesting transitions among them as the parameters change. By realizing such systems in a nonreciprocal circuit, we experimentally observe the degeneracy features of the swallowtail. Furthermore, transitions among different types of singularities complying with the topological constraints associated with them are demonstrated both theoretically and experimentally.

The three-state non-Hermitian Hamiltonian we consider takes the following form:

$$H = \begin{bmatrix} -f_1 - f_2 + 1 & -f_1 & -f_2 \\ f_1 & f_1 + f_3 & -f_3 \\ f_2 & -f_3 & f_2 + f_3 \end{bmatrix} \tag{1}$$

where f_1, f_2 and f_3 are real numbers, specifying three degrees of freedom and defining a 3D parameter space. Such a Hamiltonian preserve two symmetries[1]:

$$\eta H \eta^{-1} = H^{\dagger}, \quad [H, PT] = 0 \tag{2}$$

Here, the metric operator η=diag(–1,1,1), and the first relation shows that H is η-pseudo-Hermitian. The PT-symmetry operator is a combination of the parity-inversion P and time-reversal T operators. If the parameters f_1, f_2 and f_3 are momentum-space coordinates, then the PT operation takes the complex conjugate of the Hamiltonian up to a unitary transformation, $PT(H)=U^{\dagger}H^{*}U$, and the requirement of a real-valued Hamiltonian [Eq. (1)] is equivalent to that the Hamiltonian preserves the PT symmetry (see more details in Section 3 of the supplementary information). We note that two pairs of off-diagonal entries are anti-symmetric (H_{12}=–H_{21}, H_{13}=–H_{31}), representing nonreciprocal hopping between modes. In contrast, the remaining pair of off-diagonal entries are symmetric (H_{23}=H_{32}) and represents reciprocal hopping. The degenerate surfaces and lines in the eigenvalue structure form a swallowtail, as shown in Fig. 1a (see the ADE description in Section 2 of the supplementary information and different views of Fig. 1a in Movie 1). The ESs (red surfaces) and EL3s (black lines) result from the PT symmetry[9] of the system. The pair of EL3s merges at the MP (marked by a red star in Fig. 1a), which emits the nondefectively degenerate NL and NIL (blue lines) in opposite directions (MP is a three-fold degeneracy with two linearly independent eigenstates). The NL is isolated from ESs, and it is a linear degeneracy between the 1st and 2nd bands. In contrast, the NIL is a complete intersection of ESs[8,11,12], which are formed by the degeneracy of the 2nd and 3rd bands. The common feature is that both the NL and NIL are linear crossings of eigenvalue dispersions, and both are nondefective twofold degeneracies (i.e., the two degenerate eigenstates are linearly independent of each other). Owing to the two symmetries of the system in Eq. (2), the NL and NIL cannot be extended into a tube or cone in parameter space. Thus, their stability is symmetry-protected (see Sections 5–7 in the supplementary information for a demonstration). Therefore, the swallowtail is an assembly of different types of singularities (ES, EL3, NIL, NL and MP), and its existence is protected by the two symmetries [Fig. S4 of supplementary information shows various structures resulting from combinations of swallowtails by changing the Hamiltonian form in Eq. (S13) without breaking the symmetries in Eq. (2)].

We next analyze the local structure of eigenvalues over the swallowtail. The EL3s are lines at which two ESs meet, forming cusps. In catastrophe theory, a cusp is formed due to the projection of a bending curve (or surface) onto a lower-dimensional space. Figure 1b shows that such a bending process can be observed in non-Hermitian eigenvalue structures, i.e., on the plane f_3=0.3, the red line (ES) bends in the f_1-f_2-Reω space (ω denotes the eigenvalues). Thus, swapping of eigenvalues will occur if a tracking point moves along the ES and “jumps” through an EL3, from the ES on one side of the EL3 to the ES on the other side, as the parameters change. Here, a “jump” corresponds to a quotient map in mathematics, and details are given in Section 9 of the supplementary information (discussions in Fig. S10e1). In contrast to the EL3s, the NIL is a transversal intersection of two ESs, and the nearby eigenvalue dispersion forms a double cone (inset of Fig. 1b). The pair of EL3s and the NIL are connected by ESs, forming a loop. Tuning of the parameters (i.e., to f_3=0.1214) can shrink the loop in a continuous way until the EL3s and NIL merge at the MP (Fig. 1c). From the other direction along the f_3-axis, the MP can also be understood as a point of collision for a ray (NL) towards a surface (ES). Before the collision, points on the NL are isolated from the ES (Fig. 1d with f_3=0.01). As the NL and ES share the 2nd band (blue surface), the tuning of system parameters can make them collide, when the three eigenvalues coalesce at the MP (Fig. 1c).

To observe the exotic swallowtail configuration and investigate the topological origin of the evolution of degeneracy features in parameter space, we employ a nonreciprocal electric circuit system emulating the interaction of three modes (labeled **A**, **B** and **C** in Fig. 2) as a realization of the three-state non-Hermitian Hamiltonian. Benefiting from a wide range of active circuit elements, such as operational amplifiers, a circuit system is more flexible than other platforms, which suits our needs to accurately control the gain and loss and implement nonreciprocal hoppings. The behavior of a circuit system can be described by the Laplacian $\mathbf{I} = \boldsymbol{J}\mathbf{V}$, where $\mathbf{I}$ is the vector of input currents, $\boldsymbol{J}$ is the admittance matrix, and $\mathbf{V}$ is the vector of node voltages.[20] The matrix $\boldsymbol{J}$ plays the role of the Hamiltonian matrix. Its eigenvalues, namely admittance bands j, represent the energy spectra. Thus, the synthetic dimensions of the parameter space, f_1, f_2 and f_3, can be mapped to the tight-binding hopping parameters between each pair of circuit nodes (Fig. 2a). The circuit element structure is shown in Fig. 2b. The nonreciprocal hopping $\pm f_1$ (resp. $\pm f_2$) between **A** and **B** (resp. **A** and **C**) is implemented and precisely controlled by an impedance converter with current inversion (INIC) in tandem with the capacitance element C_1 (resp. C_2) as in Fig. 2c. The details of the INIC are given in Section 1.1 of the supplementary information. The pure capacitance element C_3 realizes a reciprocal hopping $-f_3$ between **B** and **C**. One can select the values of

C_1, C_2 and C_3 in the experiments to implement the required parameters f_1, f_2 and f_3, respectively. A photo of the printed circuit board (PCB) for the experiments is presented in Fig. 2d. By measuring the voltage response at each node to a local a.c. current input, we acquire the admittance eigenvalues and eigenstates. More details on the experimental design are shown in Section 1 of the supplementary information.

Figure 3a1 shows the ESs, EL3s and NIL obtained from the experimental measurements (solid dots) along the computed intersecting curve of the swallowtail with the plane f_3=0.3. These singularities are extracted from the measured admittance eigenvalues (marked by circles in corresponding colors, Fig. 3a2), which are functions of f_1, along various lines $f_2=f_1+s$ on the plane f_3=0.3. The ESs can be clearly recognized from the quadratic coalescence of two eigenvalues in the experimental results. Two ESs, one formed by the 1st and 2nd bands and the other formed by the 2nd and 3rd bands, meet at the cusps of EL3s, each of which is experimentally observed as the merging point of all three eigenvalues. On the other hand, the NIL is the intersection of two transversal ESs, both formed by the 2nd and 3rd bands, as indicated in Fig. 3a1. In contrast to the quadratic coalescence above, it is observed as a linear degeneracy in the eigenvalue dispersion (Fig. 3a2). The regions shaded in grey are *PT*-exact phase domains, while the unshaded regions denote *PT*-broken phases. From here, as f_3 decreases to 0.1214, the exact phase domain enclosed by the ESs shrinks to the MP (Fig. 3b1), which is the coincidence point of the linear degeneracy and the quadratic coalescence of eigenvalues (Fig. 3b2). With further lowering of f_3 to 0.01, the point on MP and ES are decoupled into an isolated point (NL) and a smooth curve (ES) as in Fig. 3c1. Correspondingly, the measured admittance eigenvalues in Fig. 3c2 indicate that the NL is a linear degeneracy of the 1st and 2nd bands, while the ES is formed by the 2nd and 3rd bands. Evidently, the MP plays a pivotal role in linking all these degeneracy lines. To more directly observe how the degeneracy lines and surfaces are connected at the MP, we further measured the eigenvalues on the plane $f_1=f_2$ (yellow plane, Fig. 1a) which contains all of them. Figure 3d1 illustrates that the NIL and NL are smoothly connected by the MP, which also serves as a tangent point to the ES. This point separates the ES into upper and lower parts, which are formed by the degeneracies of different bands (Fig. 3d2).

We now explain topological aspects of the above transitions among different singular lines. The swallowtail affords several transition processes among symmetry-protected degeneracies (see Sections 5–6 in the supplementary information). Here, we focus on the most interesting transition, i.e., from the pair of EL3s to the NIL and NL. Our goal is to demonstrate that the pair of EL3s is topologically equivalent to the NIL and NL. Let us consider a loop encircling the pair of EL3s (l_α in green on the plane f_3=0.3, Fig. 4a1) and a loop which encloses both of the NIL and the NL (l_β in yellow on the plane f_1+f_2=0.3, Fig. 4b1). Both loops inevitably cut through the ESs, as the EL3s and NIL are hypersurface singularities. Such an approach employs mathematical notions of intersection homotopy[33]. It is different from the usual homotopical descriptions using encircling loops along which all the Hamiltonians are gapped (see details in Section 6 of the supplementary information). The two loops share the same starting point (SP, purple dots) so that a direct comparison can be performed. The equivalence between l_α and l_β is manifested by observing the eigenframe rotation and deformation processes. The concept of frame rotation has been used to label different NLs in multiband Hermitian systems with PT symmetry,[17,18] in which the eigenstates form orthogonal bases of a Euclidean-like space. Here, in our non-Hermitian system, Euclidean-like geometry is no longer applicable. The symmetries in Eq. (2) require that the eigenstates satisfy the following orthogonality relation:

$$\varphi_m^T \eta \varphi_n \begin{cases} = 0 & m \neq n \\ \neq 0 & m = n \end{cases} \tag{3}$$

where the superscript T denotes transposition. Since η has the same form as the Minkowski metric and the Hamiltonian is PT-symmetric (Eq. (1)), the eigenstates φ_m are analogous to the frame fields in general relativity[34], replacing Euclidean-like geometry with Riemannian-like geometry. Hence, the eigenstates will undergo Lorentz-like transformations as the parameters vary (see details in Sections 5–6 of the supplementary information), which induce both frame rotation and frame deformation.

The trajectories of the eigenvalues along the loops l_α and l_β are shown in Figs. 4a2 and 4b2, respectively. The corresponding evolutions of eigenstates are indicated by the trajectories of the ball markers in Figs. 4a3 and 4b3, where the three axes denote the three components of the eigenstates. The experimental and theoretical results are shown in the upper and lower panels, respectively. The three eigenstates φ_1, φ_2 and φ_3 are marked with red, blue and black, respectively, colors corresponding to those of the eigenvalues with which they each associate. The increase in the markers' size denotes the evolution process as the parameters vary along each loop in the indicated direction. The eigenstates (according to normalization of Eq. (S26) in the supplementary information) need to be rescaled to place the tip of the vector on the complex unit sphere. Since we gauge the initial eigenstates to be real at the SP, the initial and final imaginary parts of the eigenstates are all zero. Thus, the evolution of the imaginary parts is simply an intermediate process under such normalization, which is convenient for characterizing the topology. Therefore, the topology is dominantly characterized by the evolution of the real parts of the eigenstates, which determines the rotation direction and rotation angle of the eigenframe. Along both loops, the accumulated rotation angle of φ_2 (in blue) is zero, and both φ_1 and φ_3 rotate by an angle of π, i.e., they each evolve from the initial states to their antipodal points (as indicated by the green radial axes), due to the PT symmetry of the system. The results show that both loops can be viewed as topologically nontrivial as the rotation angles of the eigenframe are quantized. From the SP, we observe that φ_2 and φ_3 begin to rotate in opposite directions, which is a typical frame deformation process signifying non-Hermiticity. In contrast, for *PT*-symmetric Hermitian systems, the eigenstates must rotate in the same manner during a pure eigenframe rotation.[17,18] The intermediate processes along l_α and l_β are slightly different from each other simply because they are along different trajectories. Therefore, topologically, the rotations of the eigenstates along both loops are the same, which demonstrates that l_α is equivalent to l_β, and further explains why the pair of EL3s can transition to the NIL and NL via the MP (Fig. 4c). Note that the SPs of l_α and l_β need not be the same, so the yellow and green loops in Fig. 4c need not touch in order for them to afford the same frame rotation/deformation processes (see the criteria discussed in Section 9 of the supplementary information). The continuous deformation from l_α to l_β is shown in Movie 2. The analysis indicates that the transition is topologically protected. Our method based on the Lorentz-like transformation of eigenstates also confirms that the emergence of the swallowtail is allowed by the symmetries in Eq. (2).

To summarize, we showed that the swallowtail, which plays an important role in catastrophe theory, naturally appears in the spectra of non-Hermitian systems when we considered the evolution of eigenvalues in parameter space. In a family of three-state *PT*-symmetric non-Hermitian systems with an additional pseudo-Hermitian symmetry, we found degeneracies of eigenvalues in the form of EL3s, an NIL and an NL, and these seemingly unrelated types of singularities are stably connected at an MP, forming a swallowtail. Moreover, they can convert into each other as the system parameters change. From the experimental observations and theoretical analysis, we see that the transitions occur because these singular lines are topologically associated with each other. Since the symmetries of the considered Hamiltonian play an important role in the emergence of the swallowtail, exploring the generic topological classification of these symmetry-protected catastrophe singularities in the future will be worthwhile. Meanwhile, realizing such Hamiltonians in lattice systems may provide valuable platforms for investigating the bulk–edge correspondence in non-Hermitian swallowtail gapless phases. Furthermore, transitions among diverse singularities may pave a new way for the development of sensing and absorbing devices[22,35].

Acknowledgments: This work was supported by the Research Grants Council of Hong Kong through grants AoE/P-502/20, 16307821, KAUST20SC01 (received by C. T. Chan), and 16307621 (received by H. Jia). Y. Zhu acknowledges the financial support from the National Natural Science Foundation of China (NSFC) grant 11701263. We acknowledge Prof. Zhen Lei for helpful comments in constructing the theoretical framework. Y. Zhu would like to thank Pingyao Feng for her assistance with visualizing various geometric configurations.

Author contributions: H.J. and C.T.C. planned the project. J.H., Y.W., H.J. and C.T.C. designed the sample. J.H. carried out the measurements. J.H. and H.J. analyzed the data. R.Y.Z., Y.Z. and H.J. constructed the theoretical framework. J.H., R.Y.Z., Y.Z., H.J. and C.T.C. wrote the manuscript. J.H., R.Y.Z., X.O., Y.Z., H.J. and C.T.C. contributed to the discussion.

Competing interests: The authors declare no competing interests.

Figure captions:

Fig. 1| Degeneracy features of eigenvalues on various cross sections in parameter space, showing a swallowtail structure. a, Plot of the swallowtail structure in 3D parameter space, obtained as the zero locus of the discriminant for the characteristic polynomial associated with Eq. (1). Red surfaces are ESs; blue and black lines denote nondefective (NIL and NL) and defective (EL3) degeneracy lines, respectively. The MP is denoted by the red star. **b, c,** and **d**, Eigenvalues ω (real part) on cut planes f_3=0.3 (blue), f_3=0.1214 (green) and f_3=0.01 (pink) of (**a**), respectively. Graphs of Re ω as functions of f_1 and f_2 for the three eigenvalues are in green, blue and brown, respectively.

Fig. 2| Experimental realization of the swallowtail catastrophe with a nonreciprocal circuit system. a, Tight-binding hoppings between each pair of modes **A**, **B** and **C**. **b**, Schematic diagram for realizing the Hamiltonian in Eq. (1). Nonreciprocal hoppings between **A** and **B** and between **A** and **C** in the circuit system are implemented using an INIC in tandem with capacitors; reciprocal hopping between **B** and **C** is realized with pure capacitors. **c**, Internal structure of the INIC circuit. **d**, Photo of the main part of the PCB sample for the experiments.

Fig. 3| Experimental observation of the swallowtail catastrophe with the circuit system. a–**d**, Experimental measurements of admittance eigenvalues over the swallowtail along the planes f_3=0.3 (**a**), f_3=0.1214 (**b**), f_3=0.01 (**c**) and f_1=f_2 (**d**). **a1**–**d1**, Degeneracies on these cut planes: orange-colored lines denote the ES and NL formed by the 1st and 2nd bands; olive-colored lines denote the ESs and NIL formed by the 2nd and 3rd bands. The shaded regions in grey oblique lines are *PT*-exact phases, and the unshaded regions are broken phases. The solid dots mark degeneracies experimentally identified. **a2–d2**, Real eigenvalue dispersions as functions of f_1 along various lines ($f_2=f_1+s$ or $f_3=t$) on the corresponding cut planes. The eigenvalues are ordered from small to large in exact phases. The measured admittance eigenvalues are marked in circles, and the experimental error bars of **a2** are displayed in Section 1.4 of the supplementary information. All degeneracies (EL3, ES, NIL, MP and NL) are pointed with arrows in **a2–d2**. Note that the unlabeled crossings in **b2** are not degeneracies because the imaginary parts of eigenvalues do not coincide. The imaginary parts of the eigenvalues are shown in Section 4 of the supplementary information.

Fig. 4| Understanding the transition of double EL3s to the NIL and NL from eigenframe rotation and deformation. a1-b1, The loop l_α (green) encloses the pair of EL3s, and the loop l_β (yellow) encloses the NIL and NL. **a2** and **b2**, Trajectories of eigenvalues along loops l_α and l_β, respectively. The SPs (purple dots) represent the common starting point. **a3** and **b3**, Eigenframe deformation and rotation process the along loops l_α and l_β, respectively. Upper and lower panels correspond to experimental and theoretical results, respectively. The eigenstates φ_1, φ_2 and φ_3 are colored red, blue and black, respectively. The three axes denote the three components of each eigenstate. The increase in the size of the dots denotes the directed variation in the parameters along the loops. Re and Im denote the real and imaginary parts of the eigenstates, respectively. **c**, Illustration of the transition from double EL3s to the NIL and NL in the swallowtail structure. Note that in the transition process, the loop does not cut through any degeneracy lines.

References:

1. Kawabata, K., Shiozaki, K., Ueda, M. & Sato, M. Symmetry and topology in non-Hermitian physics. *Phys. Rev. X* **9**, 041015 (2019).
2. Zhou, H., et al. Observation of bulk Fermi arc and polarization half charge from paired exceptional points. *Science* **359**, 1009–1012 (2018).
3. Kawabata, K., Bessho, T. & Sato, M. Classification of exceptional points and non-Hermitian topological semimetals. *Phys. Rev. Lett.* **123**, 066405 (2019).
4. Miri, M. A., Alu, A., Exceptional points in optics and photonics. *Science* **363**, eaar7709 (2019).
5. Bergholtz, E. J., Budich, J. C. & Kunst, F. K. Exceptional topology of non-Hermitian systems. *Rev. Mod. Phys.* **93**, 015005 (2021).
6. Tang, W., et al. Exceptional nexus with a hybrid topological invariant. *Science* **370**, 1077–1080 (2020).
7. Shen, H., Zhen, B. & Fu, L. Topological band theory for non-Hermitian Hamiltonians. *Phys. Rev. Lett.* **120**, 146402 (2018).
8. Zhang, R. Y., et al. Symmetry-protected topological exceptional chains in non-Hermitian crystals. arXiv preprint arXiv:2204.08052, 2022.
9. Delplace, P., Yoshida, T. & Hatsugai, Y. Symmetry-protected multifold exceptional points and their topological characterization. *Phys. Rev. Lett.* **127**, 186602 (2021).
10. Wang, K., Dutt, A., Wojcik, C. C. & Fan, S. Topological complex-energy braiding of non-Hermitian bands. *Nature* **598**, 59–64 (2021).
11. Xiao, Y. X., et al. Exceptional points make an astroid in non-Hermitian Lieb lattice: Evolution and topological protection. *Phys. Rev. B* **102**, 245144 (2020).
12. Sayyad, S., Stalhammar, M., Rodland, L. & Kunst, F. K. Symmetry-protected exceptional and nodal points in non-Hermitian systems. arXiv preprint arXiv:2204.13945, 2022.
13. Wan, X., Turner, A. M., Vishwanath, A. & Savrasov S. Y. Topological semimetal and Fermi-arc surface states in the electronic structure of pyrochlore iridates. *Phys. Rev. B* **83**, 205101 (2011).
14. Young, S. M. & Kane, C. L. Dirac semimetals in two dimensions. *Phys. Rev. Lett.* **115**, 126803 (2015).
15. Chiu, C. K., Teo, J. C. Y., Schnyder, A. P. & Ryu, S. Classification of topological quantum matter with symmetries. *Rev. Mod. Phys.* **88**, 035005 (2016).
16. Jia, H., et al. Observation of chiral zero mode in inhomogeneous three-dimensional Weyl metamaterials. *Science* **363**, 148–151 (2019).
17. Wu, Q. S., Soluyanov, A. A. & Bzdušek, T. Non-Abelian band topology in noninteracting metals. *Science* **365**, 1273–1277 (2019).

18. Guo, Q., et al. Experimental observation of non-Abelian topological charges and edge states. *Nature* **594**, 195–200 (2021).

19. Okuma, N., Kawabata, K., Shiozaki, K. & Sato, M. Topological origin of non-Hermitian skin effects. *Phys. Rev. Lett.* **124**, 086801 (2020).

20. Helbig, T., et al. Generalized bulk–boundary correspondence in non-Hermitian topolectrical circuits. *Nat. Phys.* **16**, 747–750 (2020).

21. Yao, S. & Wang, Z. Edge states and topological invariants of non-Hermitian systems. *Phys. Rev. Lett.* **121**, 086803 (2018).

22. Zhong, Q., et al. Sensing with exceptional surfaces in order to combine sensitivity with robustness. *Phys. Rev. Lett.* **122**, 153902 (2019).

23. Zhang, X., et al. Experimental observation of an exceptional surface in synthetic dimensions with magnon polaritons. *Phys. Rev. Lett.* **123**, 237202 (2019).

24. Okugawa, R. & Yokoyama, T. Topological exceptional surfaces in non-Hermitian systems with parity-time and parity-particle-hole symmetries. *Phys. Rev. B* **99**, 041202 (2019).

25. Kim, Y., Wieder, B. J., Kane, C. L., et al. Dirac line nodes in inversion-symmetric crystals. *Phys. Rev. Lett.* **115**, 036806 (2015).

26. Fang, C., Chen, Y., Kee, H. Y., et al. Topological nodal line semimetals with and without spin-orbital coupling. *Phys. Rev. B* **92**, 081201 (2015).

27. Ahn, J., Kim, D., Kim, Y., et al. Band topology and linking structure of nodal line semimetals with Z_2 monopole charges. *Phys. Rev. Lett.* **121**, 106403 (2018).

28. Arnol'd, V. I. *Catastrophe theory* (Springer Science & Business Media, 2003).

29. Chandrasekaran, A., Shtyk, A., Betouras, J. J. & Chamon, C. Catastrophe theory classification of fermi surface topological transitions in two dimensions. *Phys. Rev. Res.* **2**, 013355 (2020).

30. Yuan, N. F. Q. & Fu, L. Classification of critical points in energy bands based on topology, scaling, and symmetry. *Phys. Rev. B* **101**, 125120 (2020).

31. Kirillov, O. N., Overton, M., Robust stability at the swallowtail singularity. *Fron. Phys.* **1**, 24 (2013).

32. Raz, O., Pedatzur, O., Bruner, B. D. & Dudovich, N. Spectral caustics in attosecond science. *Nat. Photonics*, **6**, 170–173 (2012).

33. Gajer, P., The intersection Dold-Thom theorem. *Topology* **35**, 939–967 (1996).

34. Freedman, D. Z. & Van Proeyen, A. *Supergravity* (Cambridge Univ. Press, Cambridge, 2012).

35. Soleymani, S., et al. Chiral and degenerate perfect absorption on exceptional surfaces. *Nat. Commun.* **13**, 1–8 (2022).

Data availability: Source data of Fig.3 are provided with this paper, and the datasets generated and analysed to support this study are available at

https://drive.google.com/file/d/11nFGtefO8XpxqJ_hm0Ew2hRa8tVdvkl6/view?usp=share_link

Code availability: The code used for calculation and data processing for this paper is also available at

https://drive.google.com/file/d/11nFGtefO8XpxqJ_hm0Ew2hRa8tVdvkl6/view?usp=share_link

Additional Information:

Supplementary Information is available for this paper.

Correspondence and requests for materials should be addressed to: zhuyf@sustech.edu.cn; jiahongwei7133@gmail.com; phchan@ust.hk.

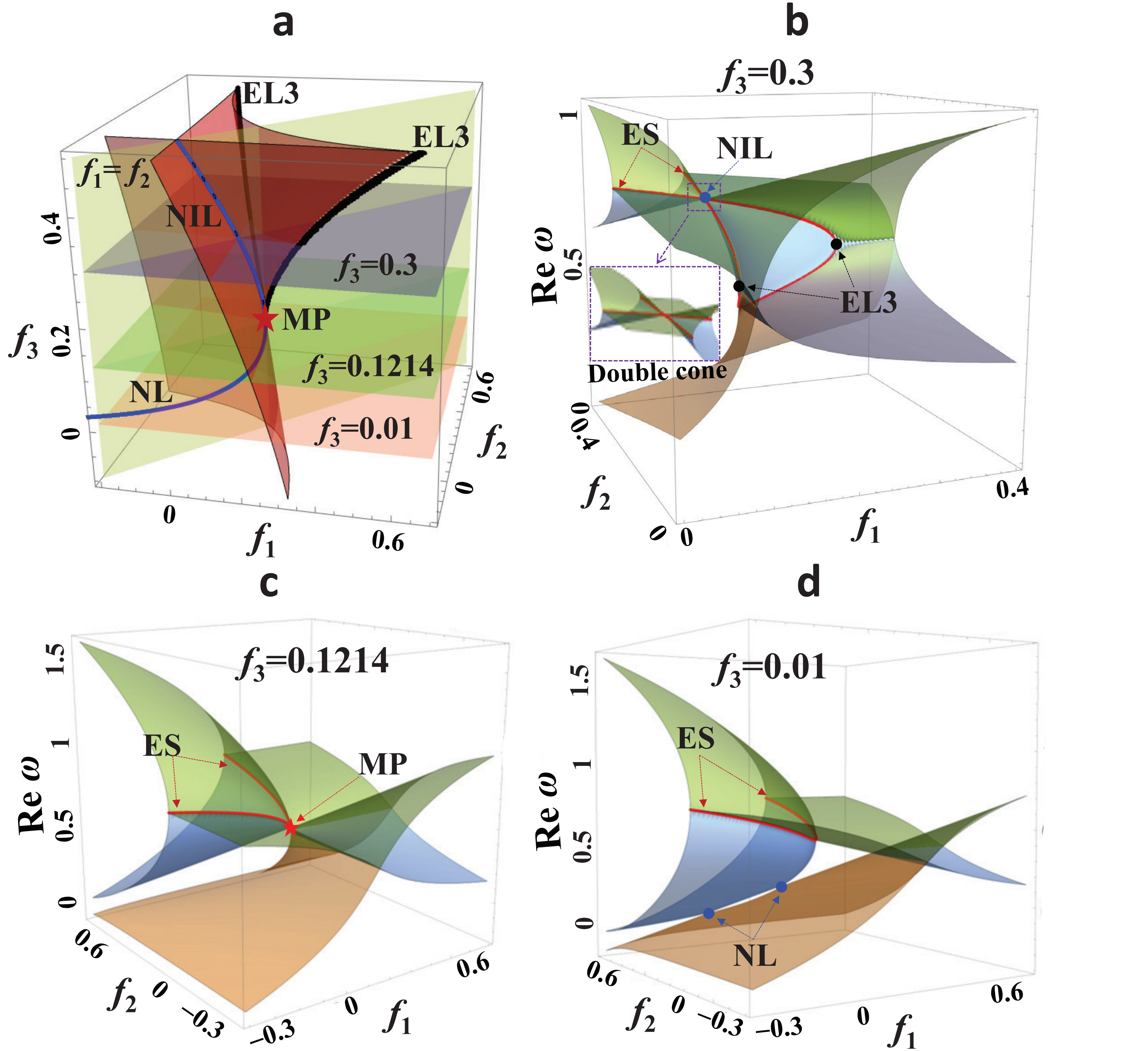

a
EL3
EL3
$f_1=f_2$
NIL
$f_3=0.3$
MP
$f_3=0.1214$
NL
$f_3=0.01$
f_3
f_1
f_2
b
$f_3=0.3$
ES
NIL
Re ω
EL3
Double cone
f_2
f_1
c
$f_3=0.1214$
ES
MP
Re ω
f_2
f_1
d
$f_3=0.01$
ES
Re ω
NL
f_2
f_1

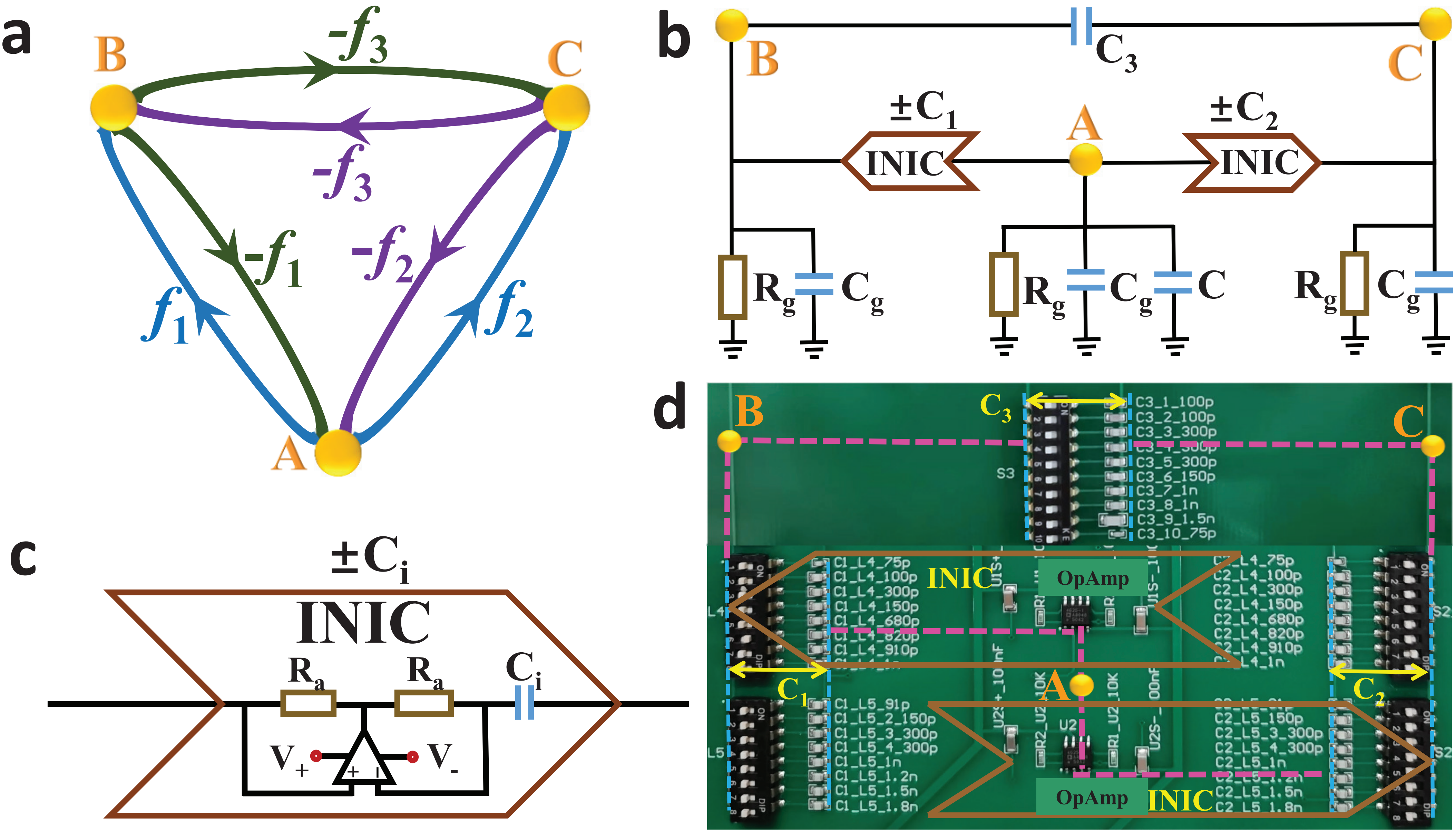

a
B
C
A
-f3
-f3
-f1
-f2
f1
f2
b
B
C
A
C3
±C1
±C2
INIC
INIC
Rg
Cg
Rg
Cg
C
Rg
Cg
c
±Ci
INIC
Ra
Ra
Ci
V+
V-
d
B
C
A
C3
C1
C2
S3
INIC
INIC
OpAmp
OpAmp
C3_1_100p
C3_2_100p
C3_3_300p
C3_5_300p
C3_6_150p
C3_7_1n
C3_8_1n
C3_9_1.5n
C3_10_75p
C1_L4_75p
C1_L4_100p
C1_L4_300p
C1_L4_150p
C1_L4_680p
C1_L4_910p
C2_L4_75p
C2_L4_100p
C2_L4_300p
C2_L4_150p
C2_L4_680p
C2_L4_820p
C2_L4_910p
C2_L4_1n
C1_L5_91p
C1_L5_2_150p
C1_L5_3_300p
C1_L5_4_300p
C1_L5_1n
C1_L5_1.2n
C1_L5_1.5n
C1_L5_1.8n
C2_L5_150p
C2_L5_3_300p
C2_L5_4_300p
C2_L5_1n
C2_L5_1.5n
C2_L5_1.8n
L4
L5
S2
U2

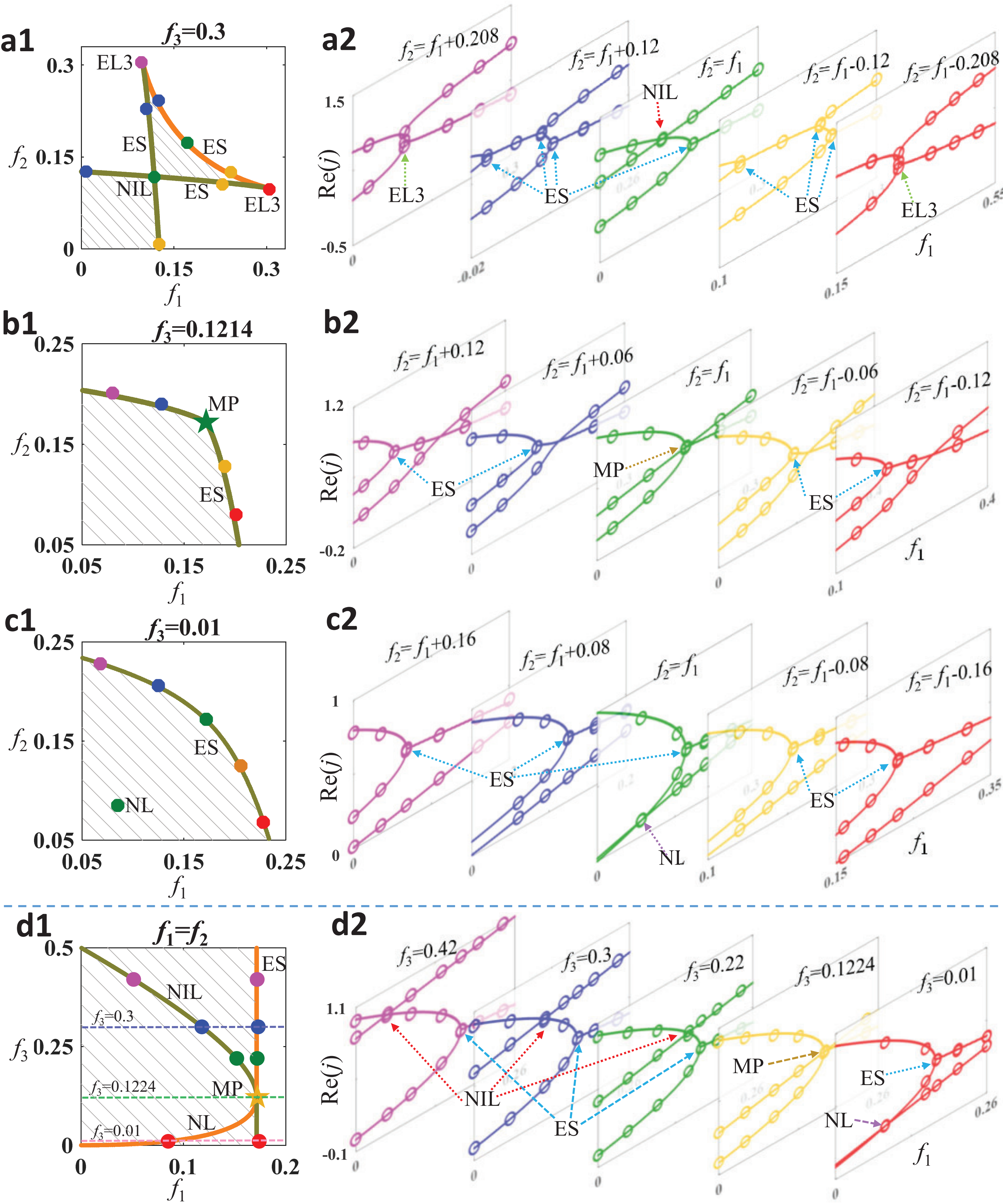

a1
f_3=0.3
EL3
ES
ES
NIL
ES
EL3
f_2
f_1
a2
f_2= f_1+0.208
f_2= f_1+0.12
f_2= f_1
f_2= f_1-0.12
f_2= f_1-0.208
NIL
EL3
ES
ES
EL3
Re(j)
f_1
b1
f_3=0.1214
MP
ES
f_2
f_1
b2
f_2= f_1+0.12
f_2= f_1+0.06
f_2= f_1
f_2= f_1-0.06
f_2= f_1-0.12
ES
MP
ES
Re(j)
f_1
c1
f_3=0.01
ES
NL
f_2
f_1
c2
f_2= f_1+0.16
f_2= f_1+0.08
f_2= f_1
f_2= f_1-0.08
f_2= f_1-0.16
ES
ES
NL
Re(j)
f_1
d1
f_1=f_2
ES
NIL
f_3=0.3
f_3=0.1224
MP
NL
f_3=0.01
f_3
f_1
d2
f_3=0.42
f_3=0.3
f_3=0.22
f_3=0.1224
f_3=0.01
NIL
ES
MP
ES
NL
Re(j)
f_1

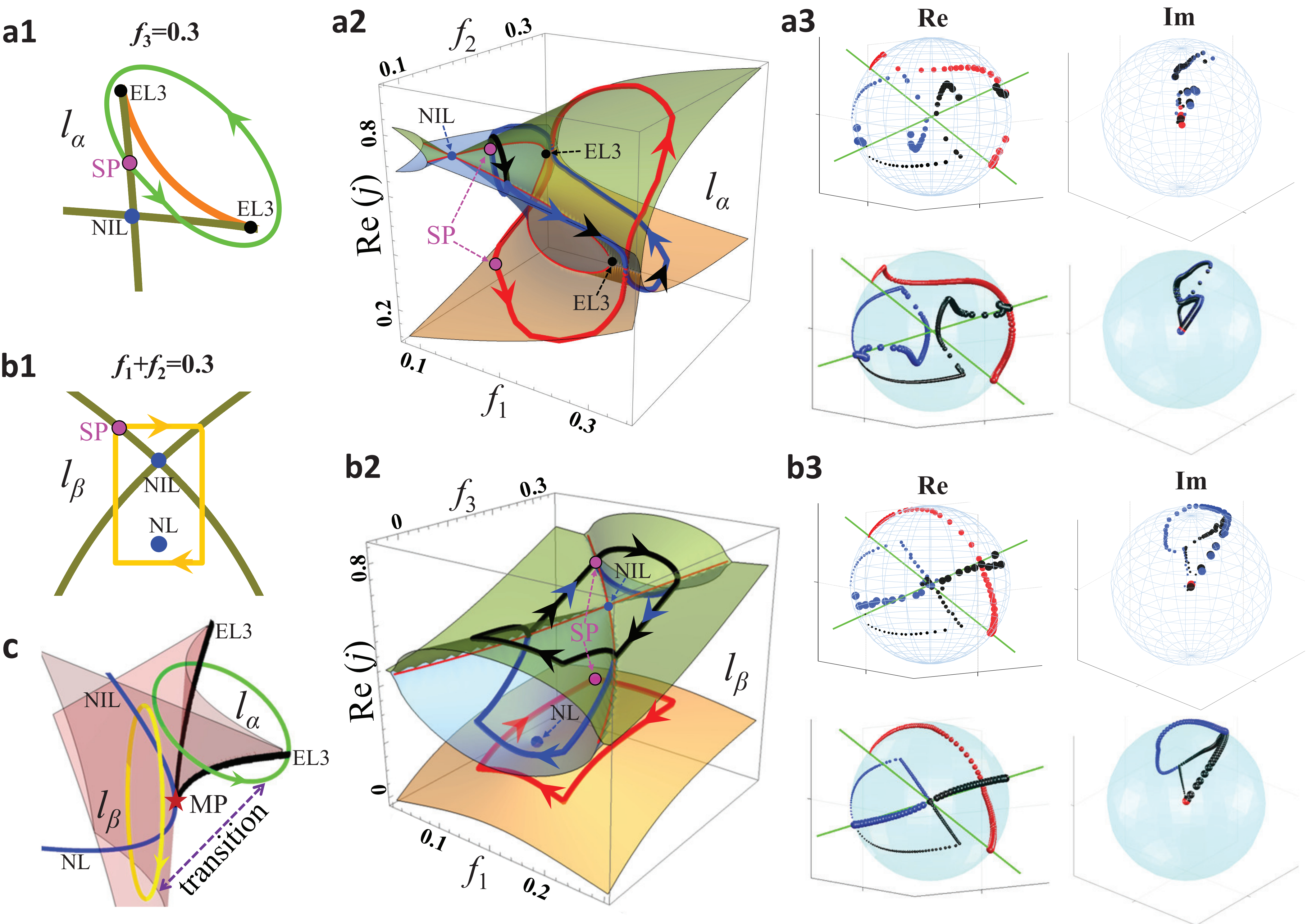

a1
f_3=0.3
EL3
l_α
SP
NIL
EL3
a2
f_2
0.3
0.1
NIL
EL3
0.8
Re (j)
SP
EL3
0.2
l_α
0.1
f_1
0.3
a3
Re
Im
b1
f_1+f_2=0.3
SP
l_β
NIL
NL
b2
f_3
0.3
0
0.8
NIL
SP
Re (j)
NL
l_β
0
0.1
f_1
0.2
b3
Re
Im
c
EL3
NIL
l_α
EL3
l_β
MP
NL
transition

Supplementary information for "Non-Hermitian swallowtail catastrophe revealing transitions among diverse topological singularities"

Jing Hu#, Ruo-Yang Zhang#, Yixiao Wang, Xiaoping Ouyang, Yifei Zhu*, Hongwei Jia*, C. T. Chan*

Content:

1. Experimental design and observation

1.1 INIC for implementing non-reciprocal hoppings

To implement non-reciprocal hoppings, we use a negative impedance converter through current inversion (INIC)[1-4], which incorporates a unity-gain stable operational amplifier (OpAmp) with two resisters R_a and R_b that are in the positive and negative feedback circuit, respectively (Fig. S1). When the OpAmp is operated stably in a negative feedback configuration, the input I_1 and output I_2 currents (depending on the node voltages V_1 and V_2) can be calculated, assuming that the negative potential is ideally equal to the positive input potential V_1

$$I_1 = -\frac{R_b}{R_a} \cdot i\omega C_i \cdot (V_1 - V_2) \tag{S1}$$

$$I_2 = i\omega C_i \cdot (V_1 - V_2) \tag{S2}$$

Here $\omega = 2\pi f$ and f is the input a.c. current of the circuit. The OpAmp, being an active circuit element, can break the circuit reciprocity. To experimentally implement the anti-symmetric parts of the Hamiltonian, R_b=R_a is required, which results in

$$I_1 = -I_2 \tag{S3}$$

It is shown that the INIC makes the admittances from the node 1 to 2 (g_{12}) and from 2 to 1 (g_{21}) opposite as follows

$$g_{12} = -i\omega C_i, g_{21} = i\omega C_i \tag{S4}$$

Viewed from node 2, the capacitance is positive (i.e. C_i), while from node 1, it behaves like a negative capacitance (i.e. $-C_i$).

1.2 The topological circuit design

For a grounded circuit, the Laplacian formalism of admittance matrix is given by[4-6]

$$J = D + W - C, \tag{S5}$$

where D denotes the total node conductance, W represents the ground matrix and C is the adjacency matrix. In our designed topological circuit with three nodes (in Fig. 2a), the total node conductance is a diagonal matrix

$$D = i\omega \begin{bmatrix} -C_1 - C_2 & 0 & 0 \\ 0 & C_1 + C_3 & 0 \\ 0 & 0 & C_2 + C_3 \end{bmatrix} \tag{S6}$$

Each diagonal element involves the sum of all components connected to the corresponding node. The adjacency matrix C is characterized by

$$C = i\omega \begin{bmatrix} 0 & C_1 & C_2 \\ -C_1 & 0 & C_3 \\ -C_2 & C_3 & 0 \end{bmatrix}, \tag{S7}$$

where the elements in the matrix determine the hoppings via capacitances between each pair of adjacency nodes. The ground matrix W reads

$$\begin{aligned} W &= i\omega \begin{bmatrix} C_g + 1/(i\omega R_g) + C_{g0} & 0 & 0 \\ 0 & C_g + 1/(i\omega R_g) & 0 \\ 0 & 0 & C_g + 1/(i\omega R_g) \end{bmatrix} \\ &= (i\omega C_g + 1/R_g)I + i\omega \begin{bmatrix} C_{g0} & 0 & 0 \\ 0 & 0 & 0 \\ 0 & 0 & 0 \end{bmatrix}, \end{aligned} \tag{S8}$$

which is also a diagonal matrix, and each element denotes the contributions from grounded capacitors (C_g and C_{g0}) and resisters (R_g) to each node. Inserting Eqs. (S6-8) into Eq. (S5) yields

$$J = (i\omega C_g + 1/R_g)I + i\omega \begin{bmatrix} -C_1 - C_2 + C_{g0} & -C_1 & -C_2 \\ C_1 & C_1 + C_3 & -C_3 \\ C_2 & -C_3 & C_2 + C_3 \end{bmatrix} \tag{S9}$$

By setting $C_1 = f_1 C_0$, $C_2 = f_2 C_0$, $C_3 = f_3 C_0, C_{g0} = C_0$, we finally arrive at

$$J=\underbrace{(i\omega C_g+1/R_g)I}_{\varepsilon_0(\omega)}+i\omega C_0\underbrace{\begin{bmatrix}-f_1-f_2+1 & -f_1 & -f_2\\ f_1 & f_1+f_3 & -f_3\\ f_2 & -f_3 & f_2+f_3\end{bmatrix}}_{\bar{J}} \tag{S10}$$

$$=\varepsilon_0(\omega)+i\omega\bar{J}$$

where the effective Laplacian $\bar{J}$ represents the effective Hamiltonian in Eq. (1) with a common divisor C_0. Here C_0 is set to be 10nF, in consideration of the magnitude of the Hamiltonian parameters and the reasonable capacitance range in the circuit system. The AC driving frequency of the system is an external parameter and was generally chosen to be 1kHz in the experiments, leaving $\omega=2\pi f$ a constant. Therefore, the parameters f_1, f_2 and f_3 can be precisely tuned by changing the capacitances C_1, C_2 and C_3, respectively. The part $\varepsilon_0(\omega)$, results from the equally grounded resistance $R_g=1M\Omega$ and capacitance $C_g=1nF$ to each node, only contributes to a complex shift of eigenvalues and does not have impact on the eigenstates.

1.3 Experimental operation and observation

The experimental sample is basically made up of surface mounted device (SMD) capacitors, resistors and OpAmps on a printed circuit board (PCB). As shown in Fig. 2b, multiple capacitors are parallelly connected between adjacent nodes, and each capacitor is connected by a serial toggle switch, so that it can be individually controlled. Hence, the capacitance C_1 (as well as C_2 and C_3) becomes a combination of the parallelly connected capacitors. The corresponding f_1, f_2 and f_3 values in the Hamiltonian are thus tunable by controlling the switches. The required capacitors (with tolerance of 1%) in experiments are listed in Table S1, and the three columns are used for tuning C_1, C_2 and C_3, respectively. Taking an exceptional point at parameter (f_1, f_2, f_3) = (0.2283, 0.1083, 0.3) as an example, it can be achieved by setting C_1=2.283nF, C_2=1.083nF and C_3 =3nF, which are decomposed as the following

C_1=43pF+560pF+ 680pF+1nF;

C_2=43pF+150pF+430pF+560pF;

C_3=1.5nF+1.5nF.

To observe this point, we simply turn on the switches of the corresponding capacitors with the above values, leaving others switches off.

In the experiments, a DC power supply (GPC-3030) served as the dual voltages of ±5V for the OpAmps (model ADA4625-1ARDZ-R7) to operate normally. A waveform generator (Keysight: M3201A) was used to excite the system and a sinusoidal voltage with constant amplitude (generally 1V~2V) and frequency of 1kHz was set to feed into each node individually. A matching oscilloscope (RS PRO IDS1074B) was employed to measure the voltage response of all nodes in the system. The input current can be acquired by connecting a shunt resistor of R=4.21 kΩ from the input node to the voltage source. With the measured voltage response to the input current vector, one can directly obtain the Green's function matrix G, which is inverse to the admittance matrix J[1-8]. The admittance eigenvalues and eigenstates are thus easily retrieved from the Green's function G.

1.4 Experimental errors

Although the experimental sample was designed exactly based on the hoppings of the tight binding Hamiltonian in Eq. 1 of the main text, slight derivations in the final experimental results from the theoretical results inevitably exist, which can be observed in Fig. 3 and Fig. 4 in the main text. The experimental errors mainly result from the parasitic capacitance and resistance of the capacitors, circuit internal resistance (switch resistance, wire resistance and welding resistance, etc.), INIC circuit (stability of the DC power supply and temperature, precision of the feedback resistance, etc.) and the measurement errors of the instrument. Here we supplement a set of experimental data with error bars that can well display the deviations from the theoretical results. Details are shown in Fig. S2, with the five panels corresponding to the panels in Fig. 3a2, respectively.

2. ADE classification of swallowtail: A_4 singularity

Before introducing the ADE classification, we first need to introduce another mathematical concept, which is the orbifold. An orbifold is much like a smooth manifold but possibly with singularities of the form of fixed points of finite group actions. A smooth manifold is a space locally modelled on Cartesian space/Euclidean spaces $\mathbb{R}^n$. An orbifold is, more generally, a space that is locally modelled on smooth action groupoids (homotopy quotients) $\mathbb{R}^n // G$ of a finite group G on a Cartesian space.

An n-dimensional orbifold is a Hausdorff topological space X, called the underlying space, with a covering by a collection of open subsets U_i, closed under finite intersections. For each U_i, there is:

1. an open subset V_i of $\mathbb{R}^n$, invariant under a faithful linear action of finite group Γ_i;
2. a continuous map φ_i of V_i onto U_i invariant under Γ_i, called an orbifold chart, which defines a homeomorphism between V_i/Γ_i, and U_i.

The collection of orbifold charts is called an orbifold atlas if the following properties are satisfied:

1. for each inclusion $U_i \subset U_j$ there is an injective group homeomorphism f_{ij}: $\Gamma_i \rightarrow \Gamma_j$
2. for each inclusion $U_i \subset U_j$ there is a Γ_i-equivalent homeomorphism ψ_{ij}, called a gluing map, of V_i onto an open subset of V_i
3. the gluing maps are compatible with the charts, i.e. $\varphi_j \psi_{ij} = \varphi_i$
4. the gluing maps are unique up to composition with group elements, i.e. any other possible gluing map from V_i to V_j has the form $g.\psi_{ij}$ for a unique g in Γ_j

The orbifold atlas defines the orbifold structure completely: two orbifold atlases of X give the same orbifold structure if they can be consistently combined to give a larger orbifold atlas. Note that the orbifold structure determines the isotropy of any point of the orbifold up to isomorphism: it can be computed as the stabilizer of the point in any orbifold chart. If $U_i \subset U_j \subset U_k$, then there is a unique transition element g_{ijk} in Γ_k such that $g_{ijk}\psi_{ik}=\psi_{jk}\psi_{ij}$. These transition elements satisfy $(\mathrm{Ad}g_{ijk}).f_{ik}=f_{jk}.f_{ij}$, as well as the cocycle relation $f_{km}.(g_{ijk}).g_{ikm}=g_{ijm}.g_{jkm}$.

An ADE singularity is an orbifold fixed point locally of the form $\mathbb{C}^n//\Gamma^*$ with $\Gamma^*\hookrightarrow SU(2)$ a finite subgroup of $SU(2)$ given by the ADE classification (and $SU(2)$ is understood with its defining linear action on the complex vector space $\mathbb{C}^2$). As is known, the finite subgroups of $SO(3)$ are exhausted by the following list:

1. the cyclic group $\mathbb{Z}_n$;

2. the dihedral group $\mathbb{D}_{2n}$, isomorphic to the semidirect product of $\mathbb{Z}_n$ and $\mathbb{Z}_2$;

3. the groups of motions of the tetrahedron, $\mathbb{T}_{12}$, of the octahedron, $\mathbb{O}_{24}$, and of the icosahedron, $\mathbb{I}_{60}$.

Let Γ be a discrete subgroup of $SO(3)$. Consider its preimage $\Gamma^*\hookrightarrow SU(2)$ under the two sheeted covering map $SU(2)\rightarrow SO(3)$. The group Γ^* is called the binary group of the corresponding polyhedron and acts on $\mathbb{C}^2$ as a subgroup of $SU(2)$. Consider the algebra of polynomial invariants of this action of Γ^*. As it turns out, this algebra is generated by three invariants x, y and z, which satisfy a single relation. This relation defines a hypersurface V in the space $\mathbb{C}^2$ with coordinates x, y and z. V is naturally isomorphic to the orbifold of the action of on Γ^* and has an isolated singular point at the origin.

For a suitable choice of generators in the algebra of invariants, the relations for the binary groups of polyhedra are as Table S2. Thus, the orbifold V of the action of a binary polyhedral group on $\mathbb{C}^2$ is isomorphic to the zero level set of the corresponding singularity.

The preimage of the singular point on V is a connected union of projective lines:

$$\pi^{-1}(0)=C_1\cup C_2\cup\cdots\cup C_\mu,\qquad C_i\cong\mathbb{CP}^1 \tag{S11}$$

The self-intersection index of each component C_i is equal to -2. Pairwise intersections are described by a graph in which a vertex is assigned by to each component C_i, and two vertices are or are not connected by an edge depending on whether the intersection index of the corresponding components is 1 or 0. In this manner one obtains the Dynkin diagrams (see Fig. S3).

The orbit of a point $x \in \mathbb{C}^{n+1}$ such that $x_1+\ldots+x_\mu=0$ under the action of the group A_μ is described by the unordered set of μ points (counting multiplicities) $x_1, \ldots, x_\mu$ on $\mathbb{C}$ and is given by the polynomial.

$$\prod_{i=0}^{\mu-1} t(t-x_i) = t^\mu + \lambda_\mu t^{\mu-2} + \ldots + \lambda_1 t + \lambda_0 \qquad \text{(S12)}$$

With the real coefficients $\lambda_i(x)$ corresponding to the parameter space.

The swallowtail is the set of zeros of the discriminant of the polynomial, and corresponds to the A_4 classification, corresponding to a quartic polynomial. The coefficients thus have three degrees of freedom λ_0, λ_1 and λ_2, and the swallowtail can be observed in the 3D space by solving zeros the discriminant. Our Hamiltonian is rather different. As it is a three-band system, the characteristic polynomial of the Hamiltonian (Eq. 1 in the maintext) is a cubic polynomial. The coefficient of the cubit term is one, and the coefficients of quadratic, linear and zeroth order terms are functions the 3D parameter space f_1-f_2-f_3. Hence, the swallowtail in the band structure cannot be described by the A_4 classification.

The formation of the swallowtail in eigenvalue dispersions is strongly correlated to the symmetries of the system (Eq. 2 in the maintext), which set a constraint to the function forms of the coefficients of the polynomial. Modifying the Hamiltonian with the symmetries preserved can lead to more complicated gapless structures, but the swallowtail can still exist. To manifest this, we study the following Hamiltonians.

$$H_1 = \begin{bmatrix} 2 & f_1 & f_2 \\ -f_1 & 0 & f_3 \\ -f_2 & f_3 & 0 \end{bmatrix},\ H_2 = \begin{bmatrix} -f_3 & f_1 & f_2 \\ -f_1 & -f_1 & f_3 \\ -f_2 & f_3 & -f_2 \end{bmatrix},\ H_3 = \begin{bmatrix} f_1 f_2 & f_1 & f_2 \\ -f_1 & f_1 & f_3 \\ -f_2 & f_3 & f_2 \end{bmatrix} \qquad \text{(S13)}$$

It is shown that all the Hamiltonians preserve the symmetries in Eq. 2. The singular lines and ESs in band structures can be obtained by solving the zeros of the discriminants of characteristic polynomials. Results are shown in Fig. S4, where Fig. S4a-c correspond to H_1-H_3 in Eq. S13, respectively. The structure in Fig. S4a exhibits four swallowtails. Within the combination, the elementary degenerate lines (EL3s, NIL and NL) can still be observed, and all the four swallowtails remain intact. Figure S4b is a little different, as can be indicated: the four swallowtails share the same MP. As a result, the nodal lines disappear. This means that within the combination process, it is possible that some swallowtails do not remain intact (i.e. some elementary degeneracy lines are annihilated). Figure S4c shows a far more complicated structure, which is a combination of more swallowtails. Intact swallowtails in the structure are labelled by cyan dashed circles.

As indicated above, the swallowtails displayed in the three-band system is rather different from that described by the A_4 ADE singularity. The characteristic polynomial is a cubic polynomial, and the coefficients do not form a 3D parameter space, but are functions of a 3D parameter space. Importantly, such general cases in mathematics have not been investigated. The frame rotation and deformation of eigenstates due to Riemannian geometry is very relevant to the symmetries of the Hamiltonian, which is a pathway for understanding the emergence of the swallowtail in band structures.

3. Parity-inversion (*P*) symmetry and time-reversal (*T*) symmetry

The *P* symmetry in our paper denotes its original meaning, i.e., the 3D parity-inversion symmetry. And accordingly, the *PT* symmetry just represents the combined symmetry of spatial inversion and time reversal. In the momentum space, the *P* and *T* operators acting on the k-space Hamiltonian $H(\mathbf{k})$ can always be expressed as

$$P[H(\mathbf{k})] = \hat{P}H(-\mathbf{k})\hat{P},\ T[H(\mathbf{k})] = \hat{\tau}H(-\mathbf{k})\hat{\tau}^{-1} \tag{S14}$$

where $\hat{P} = \hat{P}^{-1} = \hat{P}^{\dagger}$ and $\hat{\tau}^{-1} = \hat{\tau}^{\dagger}$ denote local unitary matrices acting on the internal degrees of freedom of the Hamiltonian, and H^* denotes the complex conjugate of *H*. Therefore, the combined PT operation is given by $PT[H(\mathbf{k})] = \hat{S}H^*(\mathbf{k})\hat{S}^{-1}$ with $\hat{S} = \hat{P}\hat{\tau}$. Since $(PT)^2 = \hat{S}\hat{S}^* = 1$, we know that $\hat{S} = \hat{S}^T = (\hat{S}^*)^{-1}$ is a symmetric and unitary matrix, which thus can always be decomposed as $\hat{S} = UU^T$ by a unitary matrix *U*. Therefore, for any PT-symmetric Hamiltonian in momentum space,

$H_0(\mathbf{k}) = \hat{S}H_0^*(\mathbf{k})\hat{S}^{-1}$, it can always be transformed into a real matrix by a unitary transformation: $H(\mathbf{k}) = U^\dagger H_0(\mathbf{k})U = H^*(\mathbf{k})$ (see for example [11]).

From the above analysis, we can conclude that a periodic system respects *PT* symmetry is equivalent to the fact that the Hamiltonian of the system in momentum space can always be gauged to a real matrix in a proper basis, even if we do not specify the concrete expressions of *P* and *T* operators. Therefore, for the Hamiltonian used in the present paper, if we identify the parameters f_1, f_2 and f_3 as the momentum space coordinates, the real-valued requirement of the Hamiltonian $H(f_1,f_2,f_3)=H^*(f_1,f_2,f_3)$ is equivalent to that the Hamiltonian is *PT* symmetric. However, in the real experimental system, the parameters f_1, f_2 and f_3 are synthetic dimensions representing the hopping parameters between different nodes.

4. Imaginary parts of eigenvalues

In the main text (Fig. 3), we provided the theoretical and experimental results on the real parts of eigenvalue dispersions at different cut planes in the parameter space. Here, we provide the corresponding imaginary parts on these cut planes. Results are shown in Fig. S5, where Fig. S5a-d corresponds to Fig. 3a-d in the main text, respectively. As can be indicated, the linear crossings in the panels of Fig. 3b2 (apart from the middle one) are not degeneracies. This is because these points are in the broken phase, where the real parts of the second and the third bands coincide, but their imaginary parts are complex conjugate to each other (as indicated in the panels in Fig. S5b). In addition, the other band takes real values. Thus only the real parts of the three eigenvalues coincide at these points, while their imaginary parts are different. These points are therefore different from the other degeneracies, i.e. ESs, NIL, NL, EL3s and MP. Such points with real parts of all three eigenvalues coincide lie on the “bulk-Fermi arc”, as details introduced in Section 8.

5. Riemannian geometry of evolution of eigenstates

Here we demonstrate that the evolution of eigenstates as system parameters vary is based on Riemannian geometry. The pseudo-Hermitian operator that determines the symmetry of the Hamiltonian plays a similar role to the Minkowski metric in general relativity[9]. The evolution problem is governed by the equation

$$H\left|\varphi_m\right\rangle = i\partial_\zeta \left|\varphi_m\right\rangle \tag{S15}$$

where ζ denotes a path parameter, and φ_m are the eigenstates. The completeness of eigenstates (off ES) shows that any field can be expanded as

$$\phi_n(\lambda(\zeta)) = \sum_m [U(\lambda(\zeta))]^{-1}{}_n{}^m \varphi_m(\lambda(\zeta)) \tag{S16}$$

where λ denotes the parameter space of the Hamiltonian with components $\lambda^1, \lambda^2, \lambda^3 \ldots$. It is not difficult to find that ϕ_n is also the solution of Eq. S15. In static evolution problems, $\phi_n(\lambda(\zeta))$ represents $\varphi_n(\lambda(\zeta+\delta\zeta))$. Applying the partial derivative with respect to ζ, one obtains

$$\begin{aligned} i\frac{\partial}{\partial\zeta}\phi_n(\lambda(\zeta)) &= H[U(\lambda(\zeta))]^{-1}{}_n{}^m \varphi_m(\lambda(\zeta)) \\ &= i\frac{\partial[U(\lambda(\zeta))]^{-1}{}_n{}^m}{\partial\zeta}\varphi_m(\lambda(\zeta)) + i[U(\lambda(\zeta))]^{-1}{}_n{}^m \frac{\partial\varphi_m(\lambda(\zeta))}{\partial\zeta} \end{aligned} \tag{S17}$$

The instantaneous eigenvalue problem

$$H(\lambda(\zeta))\varphi_m(\lambda(\zeta)) = E_m\varphi_m(\lambda(\zeta)) \tag{S18}$$

and applying a scalar product by the left eigenstate $\left\langle\varphi_l'\right|$ from the left of Eq. S17 yields

$$-iE_l[U(\lambda(\zeta))]^{-1}{}_n{}^l = \frac{\partial[U(\lambda(\zeta))]^{-1}{}_n{}^l}{\partial\zeta} + \left\langle\varphi_l'\right|\frac{\partial\left|\varphi_m(\lambda(\zeta))\right\rangle}{\partial\zeta}[U(\lambda(\zeta))]^{-1}{}_n{}^m \tag{S19}$$

The partial derivative with respect to ζ can be expanded as

$$\frac{\partial\left|\varphi_m(\lambda(\zeta))\right\rangle}{\partial\zeta}=\sum_k\frac{\partial\left|\varphi_m(\lambda(\zeta))\right\rangle}{\partial\lambda^k}\frac{\partial\lambda^k}{\partial\zeta},\quad (k=1,2,3...) \tag{S20}$$

We define the affine connection

$$A_k{}^n{}_m=-\left\langle\varphi_n'\right|\frac{\partial\left|\varphi_m(\lambda(\zeta))\right\rangle}{\partial\lambda^k}=-\left\langle\varphi_n'\right|\frac{\partial}{\partial\lambda^k}\left|\varphi_m\right\rangle \tag{S21}$$

and the solution to U^{-1} is thus obtained as

$$U^{-1}=\mathrm{P}\exp[\int_0^\zeta ds\frac{\partial\lambda^k}{\partial s}A_k-i\int_0^\zeta dsE(\lambda(s))]=\mathrm{P}\exp(\int_{\lambda(0)}^{\lambda(\zeta)}d\lambda^k A_k)\times\exp[-i\int_0^\zeta dsE(\lambda(s))] \tag{S22}$$

Ignoring the dynamical phase, the geometric phase is simply

$$U^{-1}=\mathrm{P}\exp(\int_{\lambda(0)}^{\lambda(\zeta)}d\lambda^k A_k) \tag{S23}$$

where P denotes path ordering operator, which is important here, because the affine connection A is a matrix. Considering the non-commutative nature of matrix product, A is a non-Abelian parallel transport gauge[9-10], and the integration of A on closed loops depends on the path circulating singularities. Here we define a local metric g with its elements being

$$g_{mn}=\left\langle\varphi_m\mid\eta\varphi_n\right\rangle \tag{S24}$$

which has explicit relations with the affine connection. The symmetries (Eq. 2 in the main text) of the Hamiltonian provide an important relation between the left and right eigenstates

$$\varphi_m'=\varphi_m^T\eta\ \text{(or equivalently, } \varphi_m'^T=\eta\varphi_m,\ \left\langle\varphi_m'\right|=\left\langle\varphi_m^*\right|\eta,\ \left|\varphi_m'\right\rangle=\eta\left|\varphi_m^*\right\rangle) \tag{S25}$$

This relation provides an orthogonality to the right eigenstates

$$\varphi_m^T \eta \varphi_n \begin{cases} = 0 & m \neq n \\ \neq 0 & m = n \end{cases} \tag{S26}$$

The orthogonal relation shows that the arbitrary phase can always be removed by normalizing the eigenstates (up to an unfixed sign)

$$\varphi_m \to \frac{\varphi_m}{\sqrt{\varphi_m^T \eta \varphi_m}} \tag{S27}$$

The normalization of eigenstates can make g a constant matrix and thus the partial derivative with respect to the path parameter vanishes

$$0 = \partial_\zeta g_{mn} = \partial_\zeta \left\langle \varphi_m \mid \eta \varphi_n \right\rangle \tag{S28}$$

Inserting the identity operator $I = \sum_l \left|\varphi_l'\right\rangle \left\langle \varphi_l\right| = \sum_l \left|\varphi_l\right\rangle \left\langle \varphi_l'\right|$, one obtains

$$\partial_{\lambda_k} \left\langle \varphi_m \mid \eta \varphi_n \right\rangle = \sum_l \left\langle \partial_{\lambda_k} \varphi_m \middle| \varphi_l' \right\rangle \left\langle \varphi_l \middle| \eta \varphi_n \right\rangle + \sum_l \left\langle \varphi_m \mid \eta \middle| \varphi_l \right\rangle \left\langle \varphi_l' \middle| \partial_{\lambda_k} \varphi_n \right\rangle \tag{S29}$$

We note that

$$\left\langle \partial_{\lambda_k} \varphi_m \mid \varphi_l' \right\rangle = \left\langle \partial_{\lambda_k} \varphi_m \mid \eta \varphi_l^* \right\rangle = \left\langle \varphi_l^* \mid \eta \mid \partial_{\lambda_k} \varphi_m \right\rangle^* = \left\langle \varphi_l' \mid \partial_{\lambda_k} \varphi_m \right\rangle^* \tag{S30}$$

and thus we have

$$0 = A_{k\ m}^{*l} g_{ln} + g_{ml} A_{k\ n}^{\ l} \tag{S31}$$

It is necessary to check if the relation still holds when we add a constant phase factor to eigenstates $\varphi_m = U_{m,f} \varphi_{m,f}$. Note that we always normalized the eigenstates to have the identity inner product $\left\langle \varphi_{m,f}' \middle| \varphi_{m,f} \right\rangle = 1$, i.e. $\varphi_m' = U_{m,f}^* \varphi_{m,f}'$ and thus $\varphi_{m,f}'^T = (U_{m,f})^2 \varphi_{m,f} \eta$. The identity operator becomes $I = \sum_l \left|\varphi_{l,f}'\right\rangle \left\langle \varphi_{l,f}\right| = \sum_l \left|\varphi_{l,f}\right\rangle \left\langle \varphi_{l,f}'\right|$, and Eq. (S30) is thus

$$\partial_{\lambda_k}\left\langle U_{m,f}\varphi_{m,f} \mid \eta U_{n,f}\varphi_{n,f}\right\rangle = \sum_l \left\langle \partial_{\lambda_k} U_{m,f}\varphi_{m,f} \middle| \varphi'_{l,f}\right\rangle \left\langle \varphi_{l,f} \middle| \eta U_{n,f}\varphi_{n,f}\right\rangle + \sum_l \left\langle U_{m,f}\varphi_{m,f} \mid \eta \middle| \varphi_{l,f}\right\rangle \left\langle \varphi'_{l,f} \middle| \partial_{\lambda_k} U_{n,f}\varphi_{n,f}\right\rangle \tag{S32}$$

It can be found that the phase factor $U^*_{m,f}U_{n,f}$ on the right hand side can be extracted, and thus Eq. S31 still holds. It is sometimes convenient to define the affine connection as (simply a replacement $\varphi'^T_{l,f} = (U_{l,f})^2 \varphi_{l,f}\eta$)

$$A_k{}^n{}_m = -\langle \varphi_n | \eta \frac{\partial}{\partial \lambda^k} | \varphi_m \rangle \tag{S33}$$

In exact phases, g is diagonal, and the phase factor $(U_{l,f})^2$ on the right hand side of Eq. S32 can be extracted, and thus Eq. S30 still holds. This important relation (Eq. S31) between the local metric g and the affine connection A reveals the Riemannian geometry of the evolution process of eigenstates as parameters vary. In the next section, we will use this equation to predict the emergence of exceptional surfaces (ESs) and nodal line (NL).

6. Predicting the emergence of NL and ESs from the viewpoint of frame rotation and deformations and the relationship with general relativity

If the metric operator η takes the identity matrix (with *PT* symmetry preserved), then the three eigenstates are all space-like and perpendicular to each other. For this case, the pseudo-Hermiticity of Hamiltonian reduces to the Hermiticity, and the anti-symmetric elements in the Hamiltonian matrix become symmetric. Such *PT* symmetric Hermitian Hamiltonians have been investigated in Ref. [11], where the eigenstates are all real and orthogonal $\langle \varphi_a | \varphi_b \rangle = 0 \ (a \neq b)$, and have positive self-inner products $\langle \varphi_a | \varphi_a \rangle > 0$. We note that such three eigenstates can form the orthonormal bases of a Euclidean space, and thus transform based on Euclidean geometry[12]. The positive inner products of eigenstates determines that the eigenstates are all space-like[9], and the transformation within these eigenstates as the system's parameters change simply induces the frame rotations[9,11,12]. As indicated by Fig. S6a, each one of the three perpendicular space-like vectors ($\vec{a}$, $\vec{b}$ and $\vec{c}$) can act as a rotation director, and the other two vectors are rotating along the director. The orthogonal relation forbids the deformation of the frame (composed of three perpendicular eigenvectors). Therefore, it is impossible that any two eigenstates become parallel to each other within the evolution process as parameters changes. Such a frame rotation of eigenstates is determined by the Hermiticity and *PT* symmetry of the system[11], which gives rise to isolated nodal lines (NL) carrying quaternion topological charges in the parameter space. However, for our case, η is replaced into a Minkowski metric form (the main consequence of non-Hermiticity), and the eigenstates are in general not perpendicular to each other, owing to the orthogonal relation defined by the indefinite inner product in Eq. (S26). One of the three eigenstates is a time-like vector $\vec{t}$ (which has a negative self-inner product $\langle \varphi_t | \eta \varphi_t \rangle < 0$, distinguished from the other space-like vectors with positive inner products), and the transformation between the time-like vector and a space-like vector (e.g. $\vec{b}$) is characterized by Lorentz boost. The Lorentz boost will result in the fact that $\vec{b}$ and $\vec{t}$ are rotating in opposite directions, which is a form of the frame deformation (ignore the scale change) distinguished from frame rotation (Fig. S6a), as indicated by Fig. S6b. Within the frame deformation process, two eigenstates can be parallel or anti-parallel to each other (Fig. S6c-d), signifying the emergence of ESs.

We first consider the *PT*-exact phase regions. In these regions, one of the three eigenstates is always imaginary, and the other two are real after the normalization by Eq. S27. For the imaginary vector, the indefinite inner product $\langle \varphi_m | \eta \varphi_m \rangle$ is negative, showing that it is a time-like vector. The other two have positive inner products $\langle \varphi_n | \eta \varphi_n \rangle > 0$, which are space-like vectors. Observing the definition of the local metric g (Eq. S24), a region that is a *PT*-exact phase may have one of the following metric forms (sequence of eigenstates are defined by ordering eigenvalues from small to large)

$$g_1 = \begin{bmatrix} 1 & 0 & 0 \\ 0 & 1 & 0 \\ 0 & 0 & -1 \end{bmatrix},\ g_2 = \begin{bmatrix} 1 & 0 & 0 \\ 0 & -1 & 0 \\ 0 & 0 & 1 \end{bmatrix},\ g_3 = \begin{bmatrix} -1 & 0 & 0 \\ 0 & 1 & 0 \\ 0 & 0 & 1 \end{bmatrix} \tag{S34}$$

It is notable that for a specific region, the local metric is invariant. The evolution of eigenstates is strongly associated with the metric form as revealed by Eq. S31. The inner product space is also the origin of Lorentz transformations as the parameters vary.

Next, we show that the Riemannian geometry can be used to predict the emergence of ES and NL. In the swallowtail catastrophe for our system, the parameter space is partitioned into three regions by the ESs, as shown in Fig. S7. Here Reg I and Reg II are the *PT*-exact phases, and Reg III is the *PT*-broken phase. We take Reg I as an example. The local metric g of Reg I can be obtained as g_1. If we gauge the imaginary vector to be real, then all the eigenstates are real, and the definition (Eq. S33) shows that the affine connection is also real. Hence, Eq. S31 reduces to

$$0 = A_{k\ m}^{\ l} g_{ln} + g_{ml} A_{k\ n}^{\ l} \tag{S35}$$

The metric is diagonal, and one can easily demonstrate that the affine connection is a linear combination of the following elementary matrices

$$T_1 = \begin{bmatrix} 0 & -1 & 0 \\ 1 & 0 & 0 \\ 0 & 0 & 0 \end{bmatrix},\ T_2 = \begin{bmatrix} 0 & 0 & 1 \\ 0 & 0 & 0 \\ 1 & 0 & 0 \end{bmatrix},\ T_3 = \begin{bmatrix} 0 & 0 & 0 \\ 0 & 0 & 1 \\ 0 & 1 & 0 \end{bmatrix} \tag{S36}$$

which are the Lie algebraic generators of SO(2,1) group. This is exactly the Lorentz transformations in 2+1D space-time in general relativity. The matrix U in Eq. S23 is the exponential of a linear combination of T_1-T_3, and is thus an element of SO(2,1) group, which is determined by the symmetries of the system (Eq. 2 in the maintext). It is shown that T_2 and T_3 characterize Lorentz boost between φ_1 and φ_3, and between φ_2 and φ_3, respectively. While T_1 characterizes the rotation of φ_1 and φ_2. It is obvious that T_1 will induce the frame rotations, while T_2 and T_3 will induce the frame deformations. We first consider the frame rotation, the π rotation of φ_1 and φ_2 is expressed by the operation

$$[\varphi_1, \varphi_2, \varphi_3]\exp(\pi T_1) = [-\varphi_1, -\varphi_2, \varphi_3] \tag{S37}$$

bringing φ_1 and φ_2 to their opposite directions, which are still the eigenstate at the same point in parameter space. Consider a closed loop on which the eigenstates adiabatically evolve and accumulate a matrix form geometric phase (πT_1 in Eq. S37). The loop simply circulates around the nodal line (NL), and the polarizations of φ_1 and φ_2 rotate π. This is a way for predicting the existence of the NL formed by the first and the second bands relating the rotation of eigenstates in a loop to the existence of singularities (degeneracies) inside the loop. In the next section, we will show that the NL cannot be extended to a tube of ES, which is symmetry protected.

The frame deformation process is more complicated, and it is strongly associated with hyperbolic transformations (Lorentz boost). However, the ES is still predictable. The Lorentz boost between the second and the third bands can be characterized by

$$[\varphi_1, \varphi_2, \varphi_3]\exp(\beta T_3) \tag{S38}$$

and the matrix exponential is

$$\exp(\beta T_3) = \begin{bmatrix} 1 & 0 & 0 \\ 0 & \cosh\beta & \sinh\beta \\ 0 & \sinh\beta & \cosh\beta \end{bmatrix} \tag{S39}$$

As β approaches +∞, we have the relation $\cosh\beta \approx \sinh\beta = \rho$, resulting in two parallel vectors

$$\begin{aligned} \varphi_1 \cosh\beta + \varphi_2 \sinh\beta = \rho(\varphi_1 + \varphi_2) \\ \varphi_1 \sinh\beta + \varphi_2 \cosh\beta = \rho(\varphi_1 + \varphi_2) \end{aligned} \tag{S40}$$

Similarly, as β approaches –∞, $\cosh\beta \approx -\sinh\beta = \rho$, one obtains another pair of anti-parallel vectors

$$\begin{aligned} \varphi_1 \cosh\beta + \varphi_2 \sinh\beta = \rho(\varphi_1 - \varphi_2) \\ \varphi_1 \sinh\beta + \varphi_2 \cosh\beta = -\rho(\varphi_1 - \varphi_2) \end{aligned} \tag{S41}$$

In gapped states, β cannot approach infinity by an integration along a path, and an infinitely large β can only be realized when a path approaches the exceptional surfaces. Consider a tracking point in the gap, β approaches infinity (say $+\infty$) as the point moves in one direction and approaches an ES, and approaches $-\infty$ at the point approaches another ES. This indicates that β varying from $+\infty$ to 0 and to $-\infty$, represents a process that a point departs from one ES and the states becomes gapped and finally arrives at another ES. The corresponding eigenstates are parallel at the initial point on the ES, bifurcate in the gap and finally evolves to two anti-parallel eigenstates on another ES. This is exactly the frame deformation process, and the key signature is that the corresponding eigenstates are rotating in opposite directions. With this deformation process, it can be assured that there will be an intersection between the two ESs (i.e. NIL). In the next section, we will show that the frame deformation can be associated with a conventionally defined Berry phase. It is notable that this process depends on the path selected, because the topology of other singularities (e.g. the NL) may participate and induces extra rotations to the eigenstates. More details will be discussed in Section 9. The eigenstates that coalesce are φ_2 and φ_3, and thus the ES, being the boundary of Reg I, are formed by the second and third bands. As such, the NIL is also formed by the second and the third bands. We note that the φ_1 and φ_3 also experience Lorentz boost, but the second band blocks the formation of ES between the first and the third bands. In Section 9, we will provide enough experimental and theoretical data for characterizing different singularities with frame rotation and deformation of eigenstates.

If we consider Reg II with metric g_2, the Lie algebraic generators will be

$$T_1' = \begin{bmatrix} 0 & 1 & 0 \\ 1 & 0 & 0 \\ 0 & 0 & 0 \end{bmatrix},\ T_2' = \begin{bmatrix} 0 & 0 & -1 \\ 0 & 0 & 0 \\ 1 & 0 & 0 \end{bmatrix},\ T_3' = \begin{bmatrix} 0 & 0 & 0 \\ 0 & 0 & 1 \\ 0 & 1 & 0 \end{bmatrix} \tag{S42}$$

meaning that ESs can be formed by the first and the second bands, or by the second and the third bands (due to frame deformation characterized by T'_1 and T'_3). The coalescence of the two ESs forms cusps, which are EL3s. We also note that there is another rotation between φ_1 and φ_3 (i.e. $\exp(\pi T'_2)$), but the first and the third bands cannot form an NL directly (blocked by the second band). Regions having the local metric g_3 is also possible, but such regions are not present in the considered parameter ranges of the Hamiltonian (Eq. 1 in the maintext). We will not give more analysis. For exact phases, regions with different local metrics are not connected, and are separated by broken phase.

The broken phases have very different forms of local metrics compared with the exact phases. In broken phases, there will always be a pair of eigenstates that are conjugate to each other, and the other eigenstate is real. The local metric in broken phase is not diagonal but is a Hermitian matrix instead. Possible forms can be (note that the eigenstates are properly normalized)

$$g_4 = \begin{bmatrix} 0 & 1 & 0 \\ 1 & 0 & 0 \\ 0 & 0 & 1 \end{bmatrix}, \ g_5 = \begin{bmatrix} 1 & 0 & 0 \\ 0 & 0 & 1 \\ 0 & 1 & 0 \end{bmatrix} \tag{S43}$$

We note that there is always a vector having a positive inner product, which is a space-like vector. The other two vectors have null self-inner products, but their mutual inner products are nonzero. Such pair of vectors are called light-like vectors in general relativity[9]. The light-like vectors were first introduced by Penrose, which is used to investigate how to bifurcate a pair of coalesced time-like and space-like vectors. It is previously imagined that light-like vectors might be found when crossing the event horizon of a black hole. Hence, the ES in parameter space might be an analog of event horizon. In the eigenvalue dispersions of our model, the light-like vectors in broken phase can be associated with one time-like vector and a space-like vector in exact phase. When a tracking point approaches ES from the exact phase, the two vectors coalesce via frame deformation, and then they bifurcate to form a pair of conjugate light-like vectors when the tracking point departure from ES to broken phase. The regions with different local metrics g in broken phase are path connected, contrary to exact phases. The boundary between these regions with different metrics is a surface with real parts of all three eigenvalues being degenerate. Such a surface is a "bulk Fermi-arc", which connects the double EL3s. This is a consequence of the swapping of eigenvalues at EL3s, as mentioned in the maintext (also see Section 8). The surface is not a degeneracy because the imaginary parts of eigenvalues are not degenerate.

7. Stability of NIL and NL under PT and pseudo-Hermitian symmetries

In this section, we demonstrate that the NIL and NL are symmetry protected and are stable in parameter space. The method in the demonstration follows[13]. We first consider the NIL (Fig. S8a). To demonstrate that the two ESs intersect stably, we need to show that the two ESs cannot be gapped, i.e. the two possible ways (shown in Fig. S8b-c) to form a gap are prohibited. In previous discussions, we defined a local metric g. The pseudo-Hermiticity of the system require that g is invariant in specific regions, and we have already shown that the g matrix in exact phases, Reg I and Reg II, are in the forms of g_1 and g_2 [see Eq. (S34)]. Thus Reg I and Reg II cannot be connected without gap closing. Therefore, the possibility of opening NIL in Fig. S8b can be excluded. Next, we consider Fig. S8c. In the previous section, we show that along a path from one ES to the other (e.g. the dark blue path in Fig. S8a), if two initially parallel eigenstates (e.g. φ_2 and φ_3) rotate in opposite directions (frame deformation, upper panel of Fig. S8e) and finally evolve to two anti-parallel states, there must be an intersection of the ESs (NIL in Fig. S8a). This can be demonstrated in view of Berry phase. Consider the vertical red loop in Rej-f_1-f_2 3D space in Fig. S8d, which is formed by joining the trajectories of the two eigenvalues along the dark blue path together (in Fig. S8a), and we concatenate the two branches of eigenstates φ_2 (blue) and φ_3 (black) as the loop passes the ESs. The frame deformation process shows that the eigenstate will rotate π along the loop (i.e. the relative rotation angle between φ_2 and φ_3, see the lower panel of Fig. S8e). If we calculate the Berry phase with the integration along the vertical loop

$$\theta = \oint -i\left\langle \varphi \middle| \nabla_f \varphi \right\rangle \tag{S44}$$

it is not difficult to show that the Berry phase is equal to the relative rotation angle π. The frame deformation is thus well connected with the conventional Berry phase. This non-trivial Berry phase shows that the loop cannot shrink to a point, and there must be a singularity (i.e. the NIL) preventing the shrinking process. Hence, the band structure in Rej-f_1-f_2 space form a lying-flat Dirac cone, and the NIL is simply the vertex (Fig. S8d), which prevents the red vertical shrinking to a point. We thus understand that the possibility of opening the NIL in Fig. S8c can be excluded. The above analysis demonstrates that the NIL is stable and is protected by the symmetries of the system.

In the previous section, we claimed that if the accumulated geometric phase of eigenstates is a matrix πT_1 (Eq. S37) along a closed loop, then the loop circulates an NL formed by the first and the second bands. Here we demonstrate that the NL, which cannot be extended to a tube of ES in parameter space, is protected by the symmetries of the system. We still take Reg I with g_1 as an example. The NL is formed by the first and the second bands, and the inner products of the corresponding eigenstates are both positive ($g_1^{11} = g_1^{22} = 1$), where the superscript indices denote the elements in g_1. To achieve our target, we need to demonstrate that these two eigenstates with the same inner products cannot form ES. At ESs, the right $|\varphi_0\rangle$ and left $|\varphi_0'\rangle$ eigenstates, and the generalized eigenstates $|\chi_0\rangle$ and $|\chi_0'\rangle$ satisfy

$$\begin{aligned} &(H(f_{ES})-\omega_0)|\varphi_0\rangle = 0, \qquad (H^\dagger(f_{ES})-\omega_0^*)|\varphi_0'\rangle = 0 \\ &(H(f_{ES})-\omega_0)|\chi_0\rangle = |\varphi_0\rangle, \quad (H^\dagger(f_{ES})-\omega_0^*)|\chi_0'\rangle = |\varphi_0'\rangle \end{aligned} \tag{S45}$$

Note that our symmetries enforce $H^\dagger = H^T$.–The eigenstates and generalized eigenstates satisfy the relations

$$\begin{aligned} &\langle\varphi_0'|\varphi_0\rangle = 0, \quad \langle\chi_0'|\varphi_0\rangle \neq 0, \\ &\langle\varphi_1'|\varphi_0\rangle = \langle\varphi_1'|\chi_0\rangle = \langle\varphi_1|\varphi_0'\rangle = \langle\varphi_1|\chi_0'\rangle = 0 \end{aligned} \tag{S46}$$

where $|\varphi_1\rangle$ (right) and $|\varphi_1'\rangle$ (left) are another pair of eigenstates with a different eigenvalue $\omega' \neq \omega_0$. The eigenstates and generalized eigenstates are generally not unique, because one can always perform the following transformations

$$\begin{aligned} &|\varphi_0\rangle \to a_0|\varphi_0\rangle, \qquad |\varphi_0'\rangle \to b_0|\varphi_0'\rangle \\ &|\chi_0\rangle \to a_0|\chi_0\rangle + a_1|\varphi_0\rangle, \quad |\chi_0'\rangle \to b_0|\chi_0'\rangle + b_1|\varphi_0'\rangle, \end{aligned} \tag{S47}$$

It is safe to introduce the orthonormal conditions to reduce the undetermined degrees of freedom[14],

$$\langle\chi_0'|\chi_0\rangle = 0, \quad \langle\chi_0'|\varphi_0\rangle = \langle\varphi_0'|\chi_0\rangle = 1 \tag{S48}$$

On ESs, the left and right (generalized) eigenstates can be associated via

$$\begin{aligned}&\eta|\varphi_0\rangle=\rho_0|\varphi_0'\rangle,\quad \eta|\varphi_0'\rangle=\frac{1}{\rho_0}|\varphi_0\rangle\\&\eta|\chi_0\rangle=\rho_0(|\chi_0'\rangle+c|\varphi_0'\rangle),\quad \eta|\chi_0'\rangle=\frac{1}{\rho_0}(|\chi_0\rangle-c|\varphi_0\rangle)\end{aligned}\tag{S49}$$

where ρ_0 and c are real under the normalization condition Eq. S48. Starting from ES, the perturbation of eigenvalues and eigenstates nearby the ES can be expressed as[14]

$$\begin{aligned}&\omega_\pm(f_{ES}+\delta f)=\omega_0\pm\sqrt{\mu(\delta f)}\delta f^{1/2}+O(\delta f)\\&|\varphi_\pm(f_{ES}+\delta f)\rangle=|\varphi_0\rangle\pm\sqrt{\mu(\delta f)}\delta f^{1/2}|\chi_0\rangle+O(\delta f)\\&|\varphi_\pm'(f_{ES}+\delta f)\rangle=|\varphi_0'\rangle\pm\sqrt{\mu(\delta f)}\delta f^{1/2}|\chi_0'\rangle+O(\delta f)\end{aligned}\tag{S50}$$

with

$$\mu(\delta f)=\langle\varphi_0'|\nabla_f H(f_{ES})|\varphi_0\rangle\cdot\delta f=\langle\varphi_0'|\partial_{f_i}H(f_{ES})|\varphi_0\rangle\cdot\delta f_i/\delta f\tag{S51}$$

where the normalization condition Eq. S48 is used, and also imposed another two normalization conditions $\langle\chi_0'|\varphi_\pm(f_{ES}+\delta f)\rangle\equiv1$ and $\langle\chi_0|\varphi_\pm'(f_{ES}+\delta f)\rangle\equiv1$. If δf takes the point off ES, we have $\mu(\delta f)\neq0$. The two symmetries of our system imply that

$$\begin{aligned}&\langle\varphi_0'|\nabla_f H(f_{ES})|\varphi_0\rangle=\langle\varphi_0'|\eta\nabla_f H^\dagger(f_{ES})\eta|\varphi_0\rangle\\&=\langle\varphi_0|\nabla_f H^\dagger(f_{ES})|\varphi_0'\rangle=\langle\varphi_0'|\nabla_f H(f_{ES})|\varphi_0\rangle^*\end{aligned}\tag{S52}$$

meaning that $\mu(\delta f)=\mu^*(\delta f)\in\mathbb{R}$. Therefore, the eigenvalues near ES should be either real if $\mu(\delta f)>0$ or form a complex conjugate pair if $\mu(\delta f)<0$. We can now calculate the inner products

$$
\begin{aligned}
&\langle \varphi_\pm(f_{ES}+\delta f)|\eta|\varphi_\pm(f_{ES}+\delta f)\rangle \\
&=(\langle\varphi_0| \pm \sqrt{\mu(\delta f)}\delta f^{1/2}\langle\chi_0|)\eta(|\varphi_0\rangle \pm \sqrt{\mu(\delta f)}\delta f^{1/2}|\chi_0\rangle)+O(\delta f) \\
&=(\langle\varphi_0| \pm \sqrt{\mu(\delta f)}\delta f^{1/2}\langle\chi_0|)(\rho_0|\varphi_0'\rangle \pm \rho_0\sqrt{\mu(\delta f)}\delta f^{1/2}(|\chi_0'\rangle + c|\varphi_0'\rangle))+O(\delta f) \\
&=(\langle\varphi_0| \pm \sqrt{\mu(\delta f)}\delta f^{1/2}\langle\chi_0|)((\rho_0 \pm c\rho_0\sqrt{\mu(\delta f)}\delta f^{1/2})|\varphi_0'\rangle \pm \rho_0\sqrt{\mu(\delta f)}\delta f^{1/2}|\chi_0'\rangle)+O(\delta f) \\
&=\pm\rho_0\sqrt{\mu(\delta f)}\delta f^{1/2}(\langle\varphi_0||\chi_0'\rangle + \langle\chi_0||\varphi_0'\rangle)+O(\delta f) \\
&=\pm 2\rho_0\sqrt{\mu(\delta f)}\delta f^{1/2}+O(\delta f)
\end{aligned}
\tag{S53}
$$

If δf takes the tracking point off ES and into exact phase (e.g. Reg I, $\rho_0 \in \mathbb{R}, \mu(\delta f) > 0$), the two eigenstates bifurcate from the eigenstates on ES must have inner products with opposite signs[13]. Thus on the boundary of Reg I, only the second and the third bands can form ES. Conversely, the two eigenstates having inner products with the same sign cannot form ES, and the degeneracy between the two eigenstates must be non-defective. We can thus understand why the NL formed by the first and the second bands is stable against expanding to a tube of exceptional points.

8. Swapping of eigenvalues and "bulk Fermi-arcs"

In non-Hermitian systems, eigenvalues may swap as the parameters vary along a closed loop. As a result, the two singularities will be connected by a bulk Fermi-arc[15]. In this section, we will discuss two examples, and the cusps (EL3s) will be included in the discussion.

We first consider a Hermitian case, i.e. the 2D Dirac points[16] or 3D nodal lines[9]. The eigenstates evolving adiabatically along a loop circulating such singularities will accumulate a π geometric phase. The final states are the same as the initial states up to a minus sigh. Within the evolution process, the sequence of eigenvalues is explicit, because the eigenvalues are always real in Hermitian systems. However, in non-Hermitian systems, the situation will be different. Let us consider a simple example, which is a two-band model, and the Hamiltonian takes the form[17]

$$H(\mathbf{k}) = (\sigma_1 + i\sigma_2) + k_x\sigma_1 + k_y\sigma_2 \tag{S54}$$

The band structure is shown in Fig. S9a, which has two isolated exceptional points (EPs) in parameter space. It can be easily found that the two EPs comes from the splitting of a Hermitian Dirac point by introducing non-Hermitian perturbations (the term $i\sigma_2$ in Eq. S54). The topology of the two EPs can be investigated by closed loops p_1 and p_2 circulating them (p_1 and p_2 have the same basepoint, the red point in Fig. S9a). By observing the evolution of eigenvalues on a closed loop circulating the EP, the two eigenvalues are braiding, resulting in a swapping $\omega_1 \leftrightarrow \omega_2$ (simultaneously $\varphi_1 \leftrightarrow \varphi_2$, see Fig. S9b-c). As a result, the eigenstates cannot evolve to the initial states after one cycle on each of the loops. However, if one considers the composite loop p_1p_2, the braiding of the eigenvalues will cancel, because the eigenvalues are braiding in opposite directions (see the red arrows in Fig. S9b-c) along p_1 and p_2. Along the composite loop, each branch of eigenstates will accumulate a π geometric phase, equivalent to the topology of a 2D Dirac point. We find that the swapping of the eigenvalues is a decomposition process. As a physical consequence, the two exceptional points are connected by a "bulk Fermi-arc", on which the real parts of all eigenvalues coalesce[15]. A loop circulating an exceptional point cannot avoid traversing the bulk Fermi-arc, which is a critical point that swaps the eigenvalues.

The EL3 is a similar example, but the swapping process is a little different compared with an isolated exceptional point. In catastrophe theory, the cusps are formed due to the folding of curves in higher dimensions[18]. In band structures, the EL3s emerge in the same way. As can be obviously indicated in Fig. 1b of the maintext, the ES is folded at the cusps in the 3D space (Reω-f_1-f_2). Hence, if a tracking point passes the EL3 along the ES, the eigenvalues experience a swapping ($\omega_1 \to \omega_{2,3}$ and $\omega_{2,3} \to \omega_1$) process. In Section 9, we will show that this swapping process is a quotient map. If the tracking point keeps moving along the ES and passes the other EL3, the eigenvalues swap back ($\omega_{2,3} \to \omega_1$ and $\omega_1 \to \omega_{2,3}$). We note that this swapping process is a little different from that of a single exceptional point, because the process involves three eigenvalues, i.e. two eigenvalues coalesce and swap with the other. This process will also lead to the "bulk Fermi-arcs". As indicated by Fig. 1b, each EL3 is connected by an arc, on which the real parts of all three eigenvalues coincide. If a tracking point cross the bulk Fermi-arc in broken phase, there will also be a swapping of eigenvalues ($\omega_{2,3} \to \omega_1$ and

$\omega_1 \to \omega_{2,3}$), acting as a critical point. It is notable that the two EL3s are connected by the same arc, because the EL3s are emitted from the same point (i.e. the MP).

9. Topologically characterizing singular lines in the swallowtail with frame deformation and rotations

The swallowtail catastrophe singularity is a typical hypersurface singularity. It includes two singularities (NIL and EL3s) that can cannot be found in Hermitian systems, and also has an NL, which has been widely observed in Hermitian systems. It is thus an intriguing phenomenon that these singular lines, which seems unrelated to each other, can mutually convert to each other via the meeting point (MP). The ESs in the swallowtail constitute a subspace of the parameter space and are singular hypersurfaces. NIL and EL3s are singularities on ES, which are higher order singularities compared with ES. Such a gapless structure is called a stratified space in topology, and the parameter space is decomposed into pieces called strata[18]. For example in the swallowtail, the first stratum is the whole parameter space, and the second stratum is the ES, being the subspace of the parameter space. The third stratum is composed of the singular lines, including NL, NIL and EL3s. Next, we provide a more detailed topological characterization of the swallowtail based on the frame deformation and rotation. Such treatment is compatible with the intersection homotopy theory[19].

Before a detailed discussion on the topological characterization, we need to introduce the following criterions on the loops and paths in parameter space:

1. The topological characterization focuses on the singular lines in the swallowtail. Hence, traversing ESs is inevitable if the enclosed singularity is a hypersurface singularity (e.g. NIL and EL3). Therefore, traversing ESs is allowed for the loops and paths, but traversing the singular lines (including NIL, NL and EL3) is not allowed.

2. If a loop traverses the ESs, it will be segmented into several paths that are located in different regions. The evolution of eigenstates along each of these paths can be described by the frame deformation and

rotation processes. The evolution along the loop is thus the combination of these processes (e.g. Fig. 4a-b in the maintext).

3. It is sometimes necessary to investigate loops or paths that are partially located on ESs, and the hypersurface singularities (e.g. NIL and EL3) partition these loops or paths into several segments. These segments are concatenated via quotient maps under equivalence relations. The quotient map does not mean that the loop or path passes the NIL or EL3 directly, which thus does not contradict criterion 1. Details on the quotient maps will be introduced in the following (mainly for loops l_2l_2' and l_3 in Fig. S10b, and l_4l_4' and l_5 in Fig. S11a).

4. If a loop can be continuously deformed to another one without encountering singular lines (NL, NIL and EL3), the two loops are equivalent. Equivalent paths are defined in the same way, and additionally, the starting points (and ending points) of the two paths are required to be consistent. Encountering ESs within the deformation process of the loops (or path) does not change the topology.

We next investigate the topology of the singular lines under the four criterions. We put the swallowtail into a sphere (Fig. S10a), so that all the singular lines and ESs can be projected onto the spherical surface viewing from the center (i.e. the MP, Fig. S10b). Among all the singular lines, the NL should be the simplest case, because it is totally isolated from the ESs. It can be enclosed by the loop l_1 (see Fig. S10b), on which the measured eigenvalues j_1, j_2 and j_3 are shown in Fig. S10c1 with red, blue and black balls respectively, falling on the computed bands (orange, blue and green surfaces) from Eq. (1) in the main text. The corresponding frame rotation of eigenstates φ_1, φ_2 and φ_3 (red, blue and black balls respectively) obtained from the experiments is shown in the upper panel of Fig. S10c2, with the theoretical results in the lower panel for comparison. Note that for NL, the frame rotation is dominant, as discussed in Section 6. The increase of ball size denotes the variation of parameters from the beginning to the ending points along the loop. It can be observed that φ_1 and φ_2 rotate π in the same direction, similar to the quaternion rotation[11].

Different from the NL, the NIL and EL3s are hypersurface singularities, the characterization of their topology would be much more complicated. The loops enclosing such singularities will be considered as a concatenation of several paths (or loops), and each of these paths (or loops) will be confined in a single region. Importantly, these paths (or loops) can be terminated at ESs, or partially located on ESs, which is compatible with our frame deformation method. It is necessary to introduce the paths (or loops) that are confined in a single region before we further discuss closed loops that are formed by the combinations of them. We firstly focus on the exact phases. The NIL is a complete intersection of ESs, and its topology in the exact phase is characterised by the loop l_2l_2' in Fig. S10b. This loop should be understood as the concatenation of two paths l_2 (lower region) and l_2' (upper region), both of which are partially located on ESs as indicated by Fig. S10b. Note that we do not call l_2 and l_2' loops because the two terminal points of l_2 (and l_2') infinitely approach the NIL along the ES. This means that the terminal points are on different ESs, having different eigenstates. *The starting point of l_2' is concatenated with the ending point of the l_2 via a quotient map. These two points have the same eigenvalues and eigenstates as they both infinitely approach the NIL along the same ES, which is an equivalence relation, and thus can be identified*. It is notable that j_1 at the ending point of l_2 is glued to j_1 at the starting point of l_2'. At the same time, the coalesced bands $j_{2,3}$ (forming ES) at the ending point of l_2 is glued to $j_{2,3}$ (coalesced, forming ES) at the starting point of l_2'. This is the criterion of the quotient map. Similarly, the ending point of l_2' can be glued to the starting point of l_2, and thus l_2l_2' forms a closed loop as a shape of "figure 8". The gluing process (quotient map) does not mean that the loop traverses the NIL, which does not contradict Criterion 1. Figure S10d1 shows that the measured eigenvalues j_2 and j_3 coalesce at the sections located on ES (red line), as expected. Contrary to the frame rotation on l_1, the eigenstates φ_2 and φ_3 along the loop l_2l_2' are observed to bifurcate in opposite directions (Fig. S10d2) and rotate $-\pi$ and π respectively, which is attributed to the Lorentz boost (mathematically characterized by Eq. S38-39). This process is exactly the frame deformation. With regard to the path l_2, the two eigenstates rotate $\theta-\pi$ and θ respectively, evolving to antipodal points on the sphere, as shown in Fig. S10d2. As an intuitive interpretation, φ_2 and φ_3 are parallel at the initial point and evolve to anti-parallel states at the ending points of l_2, which is consistent with our analysis in Section 7.

Rather than intersections, EL3s are cusps, which are geometrically treated as the projections of folded curves in higher dimensions. As we discussed previously, such folding process corresponds to the swapping of eigenvalues in band structures. In mathematics, this swapping is a consequence of a quotient map. We can take the loop l_3 as an example, which can characterize the topology of the pair of EL3s in exact phase (Fig. S10b). As can be indicated, l_3 also partially locates on ESs, and the existence of EL3s partitions the loop into several segments. To concatenate these segments, we need the quotient maps. The two points infinitely approaching the EL3 (e.g. at point Q in Fig. S10b) along the ESs have the same eigenvalues and eigenstates and can be identified. To glue the two points together, it is notable that the two coalesced bands forming exceptional points should be glued together, following the same criterion as gluing the terminal points of l_2 and l_2'. For example, the exceptional point on the lower side of Q is formed by j_2 and j_3, and should be glued to j_1 and j_2, which form the exceptional point on the upper side of Q. This gluing process is exactly the swapping of eigenvalues. Along the loop l_3, the quotient map will be operated twice at Q and P, respectively. Therefore, we can observe the swapping $j_1 \leftrightarrow j_{2,3}$ twice when the loop "passes" the EL3 (Fig. S10e1), and thus eigenvalues evolve to the initial values for one cycle along l_3. This quotient map is reasonable because the EL3s are connected by the "bulk-Fermi arcs", and the "bulk-Fermi arc" is always a critical point the swaps the eigenvalues whenever a tracking point passes it (see Section 8). Similar to $l_2 l_2'$, φ_1 and φ_3 on l_3 are rotating π in opposite directions (Fig. S10e2). At this point, we confirm that on both $l_2 l_2'$ and l_3, the eigenstates are experiencing frame deformations, which are distinguished from the frame rotation for quaternion topological charges[19]. This is a consequence of the orthogonality in Eq. S27.

In broken phase regions, the topology of NIL can be characterized by the loop $l_4 l_4'$ in Fig. S11a. Figure S11b1 shows that the real parts of eigenvalues j_2 and j_3 are degenerate, for the reason that the two eigenvalues are always conjugate in broken phases. The frame deformation is also extended to complex space. Along the path l_4, φ_2 and φ_3 experience a bifurcation process as they keep conjugate: the real parts of both eigenstates decrease to zero, and simultaneously their imaginary parts increase from zero (Fig. S11b2). As a result, the two real parallel eigenstates evolve to two imaginary ones that are anti-parallel to each other via the process (antipodal points on the imaginary sphere). This indicates that via the evolution along $l_4 l_4'$, φ_2 and φ_3 rotate π and $-\pi$ in complex space, which is still a frame deformation process as exhibited in Fig. S11b2. The topology of the double EL3s in broken phase is studied through the loop l_5 (Fig. S11b). The loop also partially locates on ESs and is partitioned by the EL3s. These segments of l_5 are concatenated via quotient maps using the same criterion as l_2 and l_2'. Hence, the swapping of eigenvalues $j_1 \leftrightarrow j_{2,3}$ occurs four times along l_5, twice of which are due to the traversing of bulk Fermi arcs, and the other twice are due to quotient maps at Q and P (see Fig. S11c1). The corresponding frame deformation of the eigenstates is shown in Fig. S11c2. We note that the accumulated rotation angles for all the eigenstates are zero, meaning that l_5 is trivial.

We then proceed to discuss the relationships of these loops. As mentioned above, along l_2 the two eigenstates (φ_2 and φ_3) are parallel at the initial points and evolve to two anti-parallel to each other at the ending point (Fig. S11d2) via a frame deformation process. However, along path l_6 (Fig. S11a), being the product of l_2 and l_1, the situation becomes very different. We can observe from Fig. S11d2 that both φ_2 and φ_3 rotate to the same point (say, the rotation angle is θ) on the sphere even though they bifurcate on the segment off ES (i.e. the two eigenstates are still parallel at the ending point of l_6). Additionally, φ_1 experiences a π rotation. This can be intuitively understood, because the topology of NL (e.g. along l_1) provides an additional π rotation to φ_1 and φ_2. Since φ_2 and φ_3 rotate the same angle and arrive at the same point along l_6, it is optional whether the two eigenstates bifurcate in the intermediate process (contrary to l_2), meaning that it is always possible to stretch l_6 so that it is totally located on ES (i.e. l_6' in Fig. S11a). From this point of view, we can determine that the NIL is a self-intersection of ES, and the NL plays a role of vortex for bending the ES. The two eigenstates can also bifurcate in the complex space, suggesting that one can continuously stretch l'_6 to the broken phase (l''_6 in Fig. S11a). All of these three loops are equivalent to each other. This indicates that encountering ES within the path (loop) deformation process does not change the topology (i.e. the final path or loop is still equivalent to the original one), which demonstrates Criterion 4. Then we come to the path l_7 (Fig. S11a and Fig. S11e1), which is the product $l'^{-1}_2 l_3 l_5$ (or simply $l'^{-1}_2 l_3$, l_5 is trivial). As shown in Fig. S11e2, along l_7, both φ_2 and φ_3 rotate θ (the same as l_6), but φ_1 rotates $-\pi$ (opposite to l_6). Thereby the relationship between l_6 and l_7 cannot be constructed directly, and the paths l_4 and l'_4 (Fig. S11a) should be employed as a bridge. On the composite path $l'^{-1}_4 l_6 l_4$ (Fig. S11f1), the rotation direction of φ_2 and φ_3 is reversed (i.e. $-\theta$) and φ_1 remains rotating π (Fig. S11f2), which is opposite to l_7, and thus one obtains a crucial relation

$$l'^{-1}_4 l_6 l_4 \simeq l_7^{-1} \text{ or } l_4 l_7 l'^{-1}_4 \simeq l_6^{-1} \tag{S55}$$

Hence, we can understand that the path $l'^{-1}_4 l_6 l_4$ ($l_4 l_7 l'^{-1}_4$) can be continuously deformed to l_7^{-1} (l_6^{-1}) without encountering any other degeneracy lines (see Fig. S11g1). This relation also ensures the following two transition processes. It can be easily derived that the loop $l_3^{-1} l_5$ ($\simeq l_7^{-1} l_2^{-1} l_5$, l_5 is trivial) enclosing the double EL3s is equivalent to $l'^{-1}_4 l_6 l_4 l_2^{-1}$ circulating the NIL and NL (Fig. S11g2). Hence, the double EL3s cannot annihilate each other, but will transit to the NIL and the NL via the MP. This equivalent relation is also demonstrated in the maintext in another decomposition method, and the consequences via the two methods are consistent. One can also derive that l_1 ($\simeq l_6 l_2^{-1}$) is equivalent to $l_4 l_7^{-1} l'^{-1}_4 l_2^{-1}$, so that the NIL and the double EL3s can merge and transit to an NL via the MP (Fig. S11g3). Taken together, it is understandable that the swallowtail originates from the topological associations amongst the degeneracy lines as aforementioned.

10. Sequence of eigenstates after traversing ES

For an isolated singularity, a common approach in characterizing its topology is simply observing the adiabatic transformation process along a closed loop enclosing it. However, if one considers a hypersurface singularity, the situation will be very different. Because a closed loop enclosing such singularities will inevitably traverse the exceptional surfaces. In characterizing the topology with eigenstates, it naturally gives rise to a problem as to how to define the order of eigenstates after traversing exceptional surfaces. In this section, we will discuss this question in detail based on the swallowtail.

We firstly consider the loop l_α, which encloses the double EL3s (Fig. S11a in the main text). In Section 9, we note that the loop can be decomposed into a product of l_3 and l_5 (Fig. S11a), and l_5 is trivial. This means that the path residing in broken phase of l_α can be totally deformed onto the exceptional surface, and thus l_α and l_3 are equivalent. Thus it can be understood that changing the order of φ_2 and φ_3 on the path residing in broken phase simply affects the intermediate evolution process but does not affect the topological characterization. In Fig. S12a1-a2, we plot the frame rotation and deformation process along l_α, and the order of φ_2 and φ_3 is exchanged on the path that resides in broken phase. Compared with Fig. 4a3 in the main text, we find that the evolution of the real parts of eigenstates follows the same trajectories. The imaginary parts of eigenstates were added by a minus sign, but the evolution of the imaginary parts is simply an intermediate process (eigenstates are real at the beginning and ending points). The topology of the double EL3s is dominantly determined by the evolution of real parts. Hence, we confirm that exchanging the order of φ_2 and φ_3 on path residing in broken phase does not affect the topological characterization of the double EL3s.

The loop l_β is partitioned into four segments by the ESs (see Fig. 4b1 in the main text), two of which reside in exact phases, and the other two reside in broken phase. To combine the four segments, we need a convention: on the two segments in broken phases, the order of φ_2 and φ_3 are unified, i.e. sorted by the corresponding eigenvalues (imaginary parts); on the two segments in exact phases, the eigenstates are sorted by the corresponding eigenvalues (from small to large). The convention ensures that the continuous deformation process of loop l_β (from Fig. 12b1-b3) is allowed. Following this convention, exchanging the order of φ_2 and φ_3 on the two segments simultaneously will not change the topological characterization by frame rotation and deformation process. As indicated by Fig. S12c1-c2.

References

1. Helbig, T., Hofmann, T., Imhof, S., et al. Generalized bulk–boundary correspondence in non-Hermitian topolectrical circuits. *Nat. Phys.* **16**, 747-750 (2020).

2. Hofmann, T., Helbig, T., Lee, C. H., et al. Chiral voltage propagation and calibration in a topolectrical Chern circuit. *Phys. Rev. Lett.* 122, 247702 (2019).

3. Chen, W. K., The Circuits and Filters Handbook (Five Volume Slipcase Set). CRC Press, 2018.

4. Lu, L., Topology on a breadboard. *Nat. Phys.* **14**, 875-877 (2018).

5. Lee, C. H., Imhof, S., Berger, C., et al. Topolectrical circuits. *Commun. Phys.* **1**, 1-9 (2018).

6. Imhof, S., Berger, C., Bayer, F., et al. Topolectrical-circuit realization of topological corner modes. *Nat. Phys.* **14**, 925-929 (2018).

7. Ningyuan, J., Owens, C., Sommer, A., Schuster, D., Simon, J., Time-and siteresolved dynamics in a topological circuit. *Phys. Rev. X* **5**, 021031 (2015).

8. Helbig, T., et al. Band structure engineering and reconstruction in electric circuit networks. *Phys. Rev. B* **99**, 161114 (2019).

9. Freedman, D. Z., Van Proeyen, A., Supergravity. Cambridge university press, 2012.

10. Schleich, W. P., Quantum optics in phase space. John Wiley & Sons, 2011.

11. Wu, Q. S., Soluyanov, A. A., Bzdušek, T., Non-Abelian band topology in noninteracting metals. *Science* **365**, 1273-1277 (2019).

12. Frankel T. The geometry of physics: an introduction. Cambridge university press, 2011.

13. Cui, X., Zhang, R. Y., Chen, W. J., et al. Symmetry-protected topological exceptional chains in non-Hermitian crystals. arXiv preprint arXiv:2204.08052, 2022.

14. Seyranian, A. P., Mailybaev, A. A., Multiparameter stability theory with mechanical applications. World Scientific, 2003.

15. Zhou, H., Peng, C., Yoon, Y. et al. Observation of bulk Fermi arc and polarization half charge from paired exceptional points. *Science* **359**, 1009-1012 (2018).

16. Young, S. M., Kane, C. L., Dirac semimetals in two dimensions. *Phys. Rev. Lett.* **115**, 126803 (2015).

17. Shen, H., Zhen, B., Fu, L., Topological band theory for non-Hermitian Hamiltonians. *Phys. Rev. Lett.* **120**, 146402 (2018).

18. Arnol'd, V. I., Catastrophe theory. Springer Science & Business Media, 2003

19. Gajer, P., The intersection Dold-Thom theorem. *Topology* **35**, 939-967 (1996).

Figures and tables

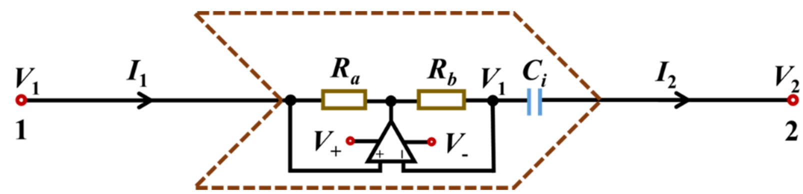

Fig. S1| Circuit diagram of a negative impedance converter structure through current inversion.

	C_1 (Num)	C_2 (Num)	C_3 (Num)
1	43 pF (1)	43 pF (1)	75 pF (1)
2	75 pF (3)	75 pF (3)	100 pF (3)
3	91 pF (1)	91 pF (1)	150 pF (1)
4	100 pF (3)	100 pF (3)	300 pF (3)
5	150 pF (4)	150 pF (4)	1 nF (2)
6	300 pF (7)	300 pF (7)	1.5 nF (3)
7	430 pF (1)	430 pF (1)	
8	470 pF (1)	470 pF (1)	
9	560 pF (1)	560 pF (1)	
10	680 pF (2)	680 pF (2)	
11	750 pF (1)	750 pF (1)	
12	820 pF (3)	820 pF (3)	
13	910 pF (1)	910 pF (1)	
14	1 nF (5)	1 nF (5)	
15	1.2 nF (2)	1.2 nF (2)	
16	1.5 nF (1)	1.5 nF (1)	
17	1.8 nF (1)	1.8 nF (1)	

Table S1| The capacitances of C_1, C_2 and C_3 mounted on the circuit for tuning f_1, f_2 and f_3, respectively.

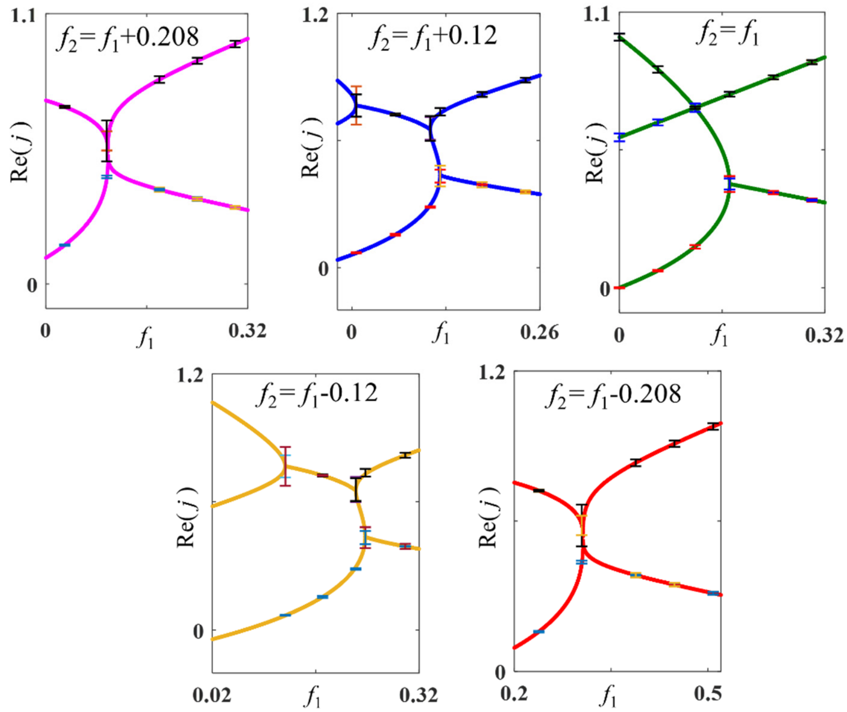

f_3=0.3

Fig. S2| Experimental data with vertical error bars that display the experimental deviations from the theoretical results, corresponding to the measured data in Fig. 3a2. At each experimental data point, the center of the error bar is the theoretical value (line), and the half length of the error bar is the absolute difference between the measured eigenvalue in Fig.3a2 and the theoretical value.

$\mathbb{Z}_n$	$x^n + yz = 0$	A_n
$\mathbb{D}^*_{2n}$	$xy^2 - x^{n+1} + z^2 = 0$	D_{n+2}
$\mathbb{T}^*$	$x^4 + y^3 + z^2 = 0$	E_6
$\mathbb{O}^*$	$x^3 + xy^3 + z^2 = 0$	E_7
$\mathbb{I}^*$	$x^5 + y^3 + z^2 = 0$	E_8

Table S2| Binary groups of polyhedral.

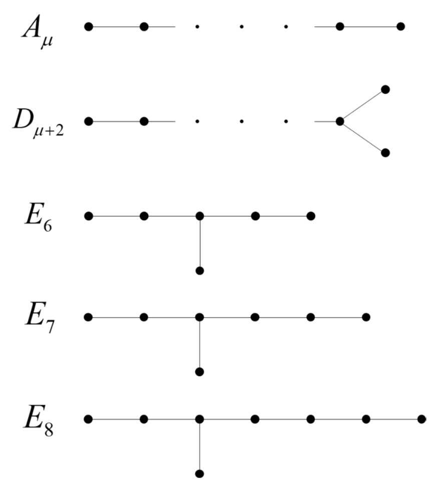

Fig. S3| Dynkin diagram.

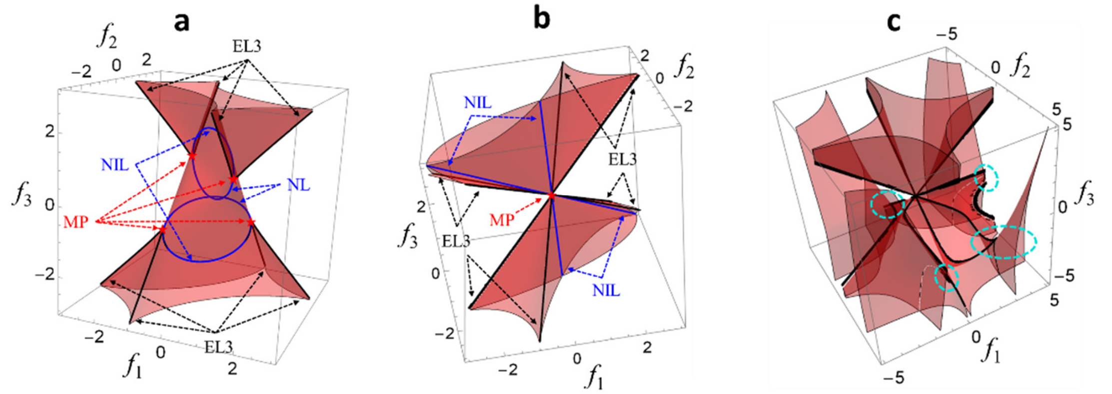

Fig. S4| Intriguing structures resulting from the combination of swallowtails. **a**, **b** and **c** are obtained by solving zeros of the discriminant of characteristic polynomial of the Hamiltonians of Eq. S13.

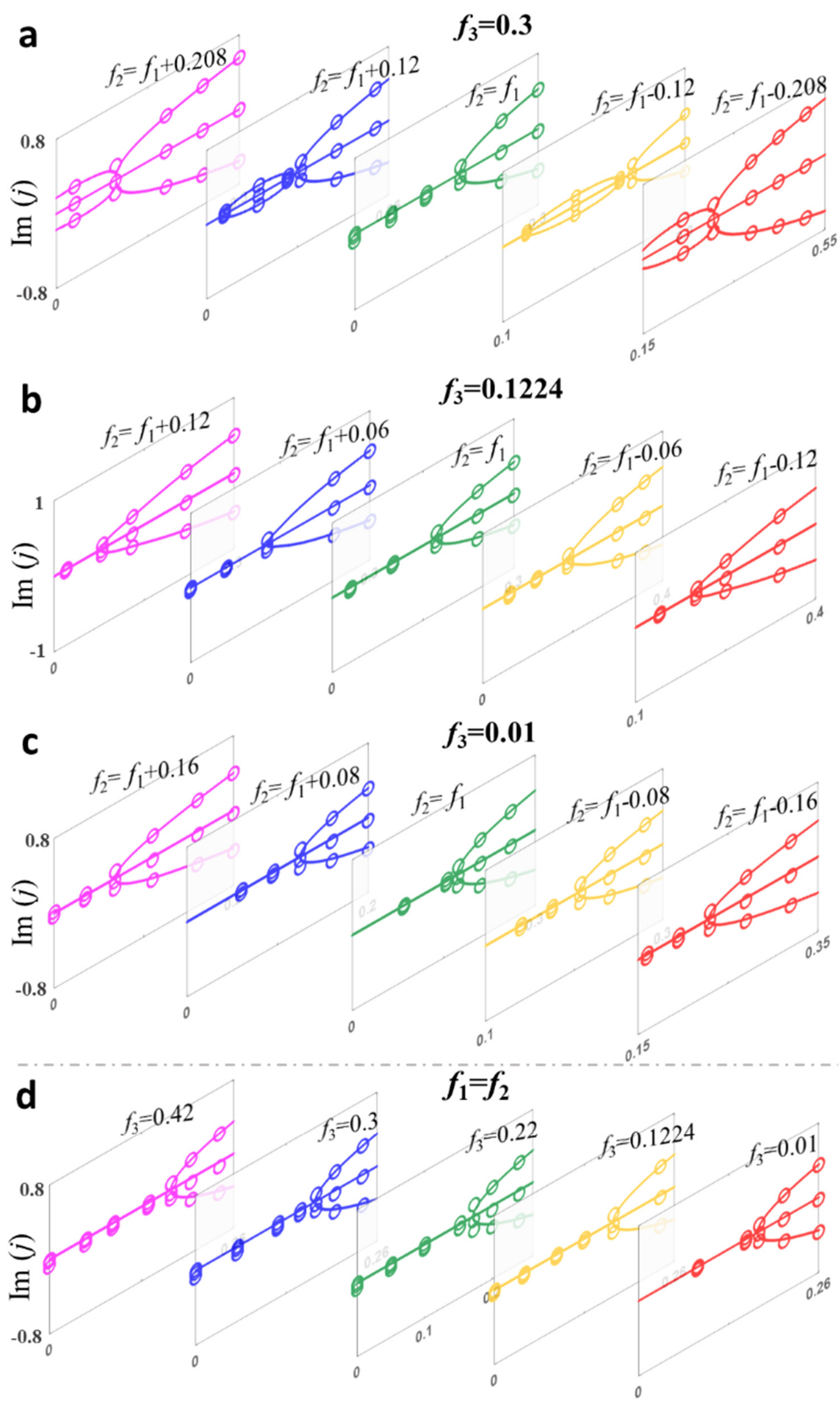

Fig. S5| Imaginary parts of eigenvalue dispersions. (a-d) correspond to Fig. 3a-d in the main text, respectively.

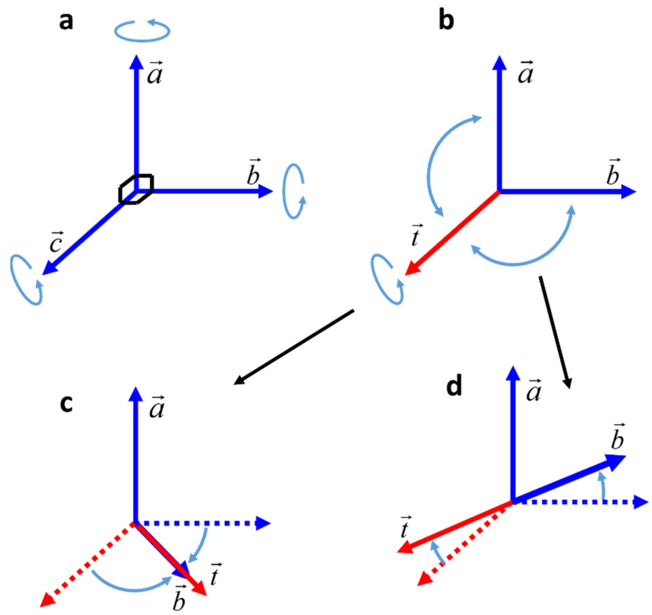

Fig. S6| Comparison between frame rotation and deformation. **a**, Frame rotation. **b-d**, Frame deformation. **c-d**, Two eigenvectors can be parallel or anti-parallel within the deformation process, signifying the emergence of ESs.

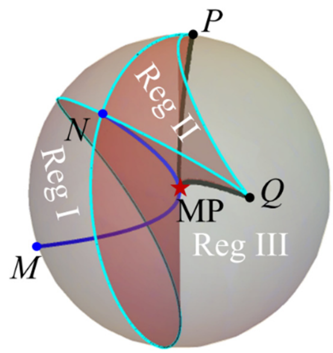

Fig. S7| Different regions partitioned by ESs. Reg I and Reg II: *PT*-exact phases. Reg III: *PT*-broken phase.

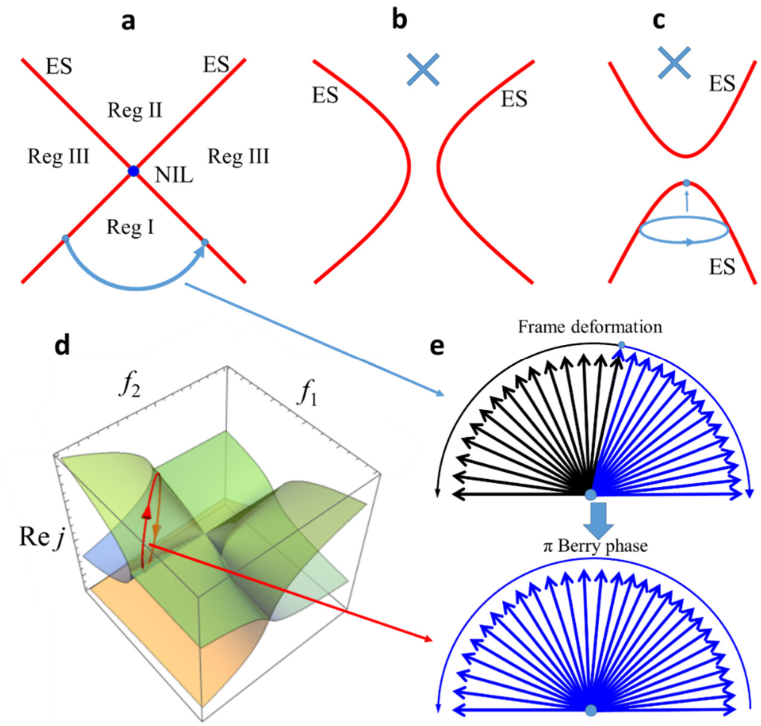

Fig. S8| Demonstration of the stability of NIL. **a**, Different areas in parameter space partitioned by the NIL (refer to Fig. S7). **b-c**, Two ways of opening the NIL to form bandgaps are prohibited. D. Band structure near the NIL. E. Upper panel: Schematic diagram of frame deformation of φ_2 (blue) and φ_3 (black) along the dark blue path in (**a**). Lower panel: Joining the trajectories of the two eigenvalues along the dark blue path (in **a**) together and concatenating the two branches of eigenstates φ_2 and φ_3 at ESs, the frame deformation process can be understood as a relative rotation angle $[\theta(\varphi_2)-\theta(\varphi_3)]$, which is equivalent to a π Berry phase accumulated by the eigenstate along the red vertical loop in **d** (Eq. S41).

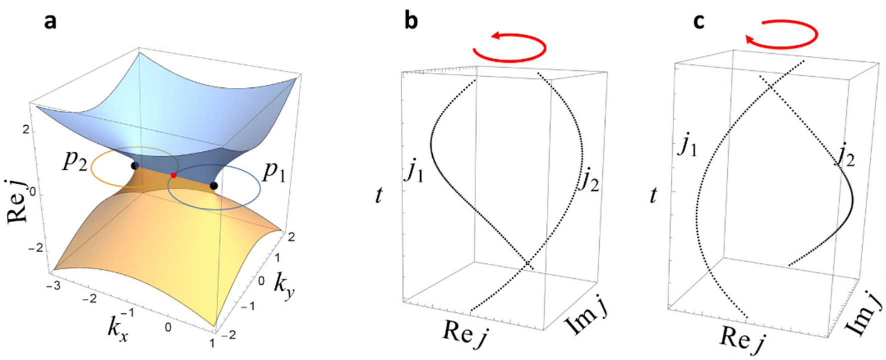

Fig. S9| Braiding of eigenvalues along loops circulating isolated exceptional points. **a**, band structure and bulk Fermi-arc. **b-c**, braiding of eigenvalues along p_1 and p_2 in (**a**).

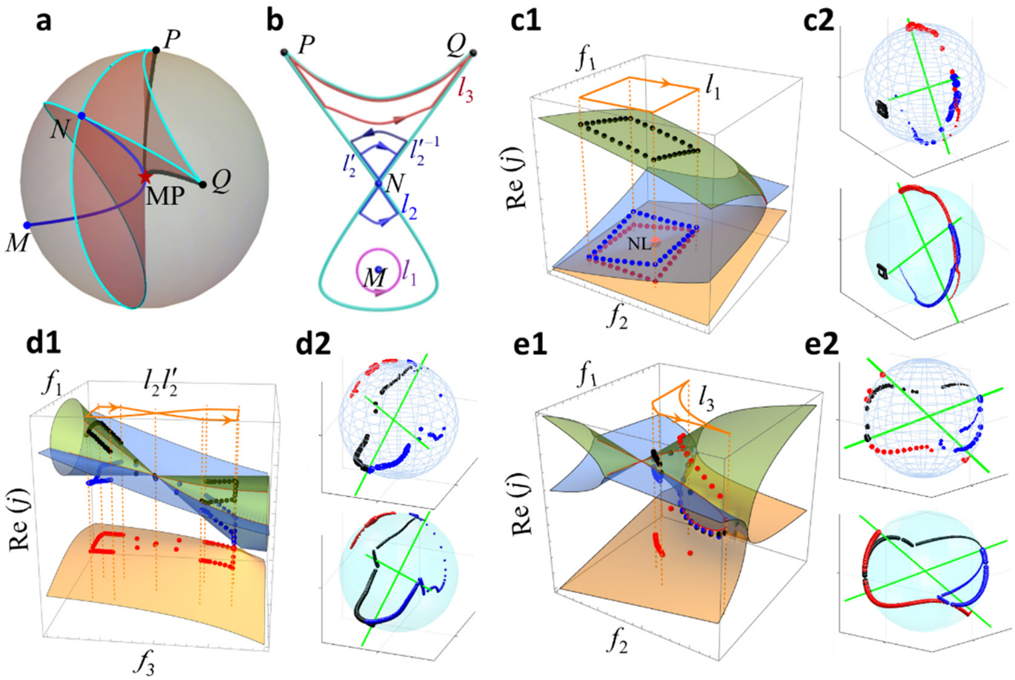

Fig. S10| Loops carrying non-trivial topology in *PT*-exact phases. **a**, Locating the swallowtail into a sphere, with MP at the center. **b**, Viewed from the centre (MP), the singular lines and surfaces are projected onto the spherical surface (extracted from **a**). The ESs are projected onto the cyan lines, the double EL3s are projected onto points P and Q, and the NIL and NL are projected onto N and M, respectively. Loops l_1 (on plane f_3=0.01), l_2 (on plane f_1+f_2=0.3) and l_3 (on plane f_3=0.3) characterize the topology of NL, NIL and double EL3s in exact phases. l_2 and l_3 are partially on ES, **c1-e1**, Band structures and evolution of eigenvalues on these loops, with points being experimental results. **c2-e2**, Frame rotation and deformation of eigenstates along these loops. The upper and lower panels are theoretical and experimental results, respectively. The gradually increasing ball size denotes the evolution process on the loops. Red, blue and black balls in (**c-e**) denote φ_1, φ_2 and φ_3 (the corresponding eigenvalues: j_1, j_2 and j_3), respectively.

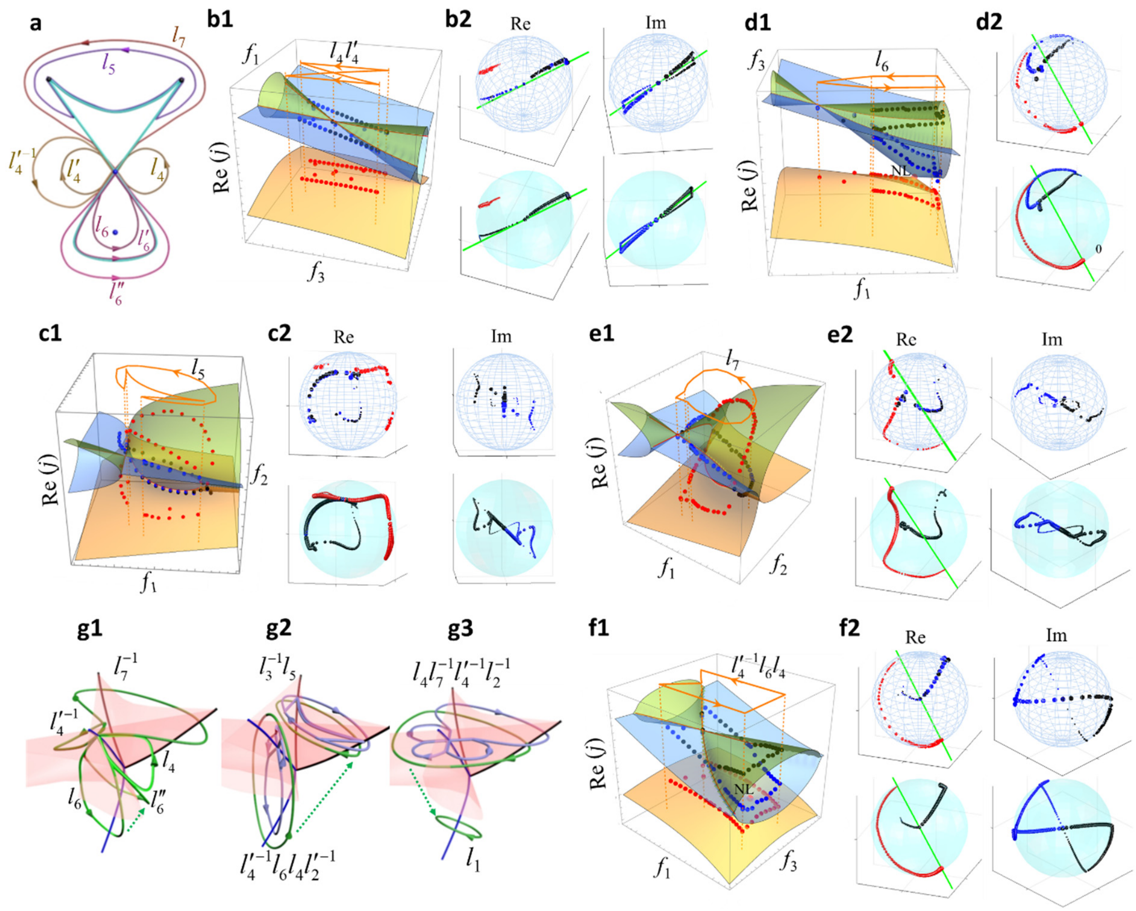

Fig. S11| Topological characterization of NIL and double EL3s in broken phases and relations between these loops. **a**, Loops circulating singularities. l_4 and l_6 are on plane f_1+f_2=0.3. l_5 and l_7 are on plane f_3=0.3. **b1-f1**, Plot of band structures on different planes, and evolution of eigenvalues on loops. **b2-f2**, Frame rotation and deformation process along these loops, where Re and Im represent real and imaginary components of the eigenstates. Red, blue and black balls in (**b-f**) denote φ_1, φ_2 and φ_3 (the corresponding eigenvalues: j_1, j_2 and j_3), respectively. **g1-g3**, Deformation of loops conserving topological charges. **g1**, $l_4'^{-1}l_6l_4$ can be deformed to l_7^{-1} by stretching l_6 to l_6'' and opening the basepoint. **g2**, The loop $l_3^{-1}l_5$ that encloses the double EL3s can be deformed to $l_4'^{-1}l_6l_4l_2'^{-1}$ circulating the NIL and NL. **g3**, The loop $l_4l_7^{-1}l_4'^{-1}l_2$ (circulating the NIL and the double EL3s) can be deformed to l_1 (circulating the NL).

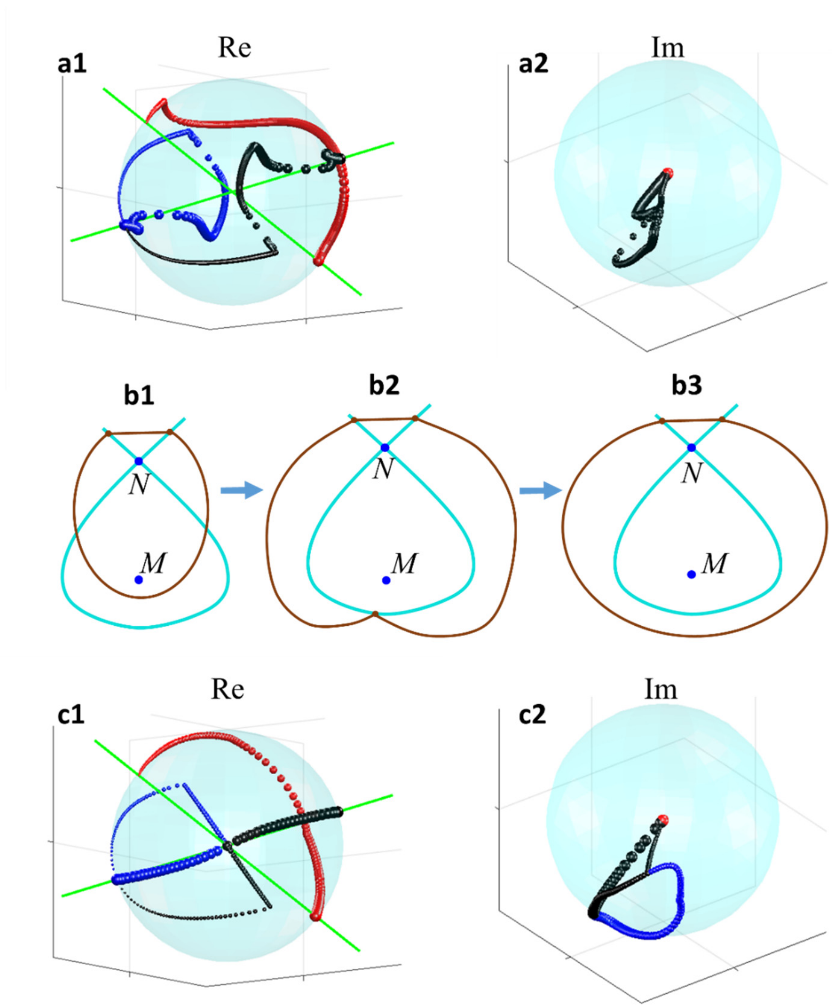

Fig. S12| Frame rotation and deformation process by exchanging the order of φ_2 and φ_3 on the path in broken phases. **a1-a2**, Frame deformation process along l_α, in which φ_2 and φ_3 exchanges on the path residing in broken phase. **b1-b3**, Continuous deformation process of loop l_β without changing the topology. **c1-c2**, Frame deformation and rotation process along l_β, in which φ_2 and φ_3 exchanges on the two segments residing in broken phases simultaneously.